A new mechanism of fibronectin fibril assembly revealed by live imaging and super-resolution microscopy.

Darshika Tomer[1], Cecilia Arriagada[1], Sudipto Munshi[2,‡], Brianna E. Alexander[1,3], Brenda French[2], Pavan Vedula[4], Valentina Caorsi[5], Andrew House[6], Murat Guvendiren[6], Anna Kashina[4], Jean E. Schwarzbauer[7], and Sophie Astrof[1,*].

1. Department of Cell Biology and Molecular Medicine, Cardiovascular Research Institute, Rutgers Biomedical and Health Sciences, 185 South Orange Ave, Newark, NJ, 07103, USA.

2. Sidney Kimmel Medical College of Thomas Jefferson University, Philadelphia, PA, 19107, USA

3. Multidisciplinary Ph.D. Program in Biomedical Sciences. Cell Biology, Neuroscience and Physiology track, Rutgers Biomedical and Health Sciences, Newark, NJ, 07103, USA.

4. Department of Biomedical Sciences, University of Pennsylvania, Philadelphia, PA 19104, USA

5. Abbelight, 191 Avenue Aristide Briand, 94230 Cachan, France

6. Otto H. York Chemical and Materials Engineering, Department of Biomedical Engineering, New Jersey Institute of Technology, Newark, NJ 07102, USA

7. Department of Molecular Biology, Princeton University, Princeton, New Jersey, USA

‡Current Address: Department of Chemical and Structural Biology, Weizmann Institute of Science, Rehovot, Israel

*Author for correspondence: Sophie Astrof, Ph.D.

Phone: 617-429-8295

E-mail: sophie.astrof@rutgers.edu

Abstract

Fn1 fibrils have long been viewed as continuous fibers composed of extended, periodically aligned Fn1 molecules. However, our live imaging and single-molecule localization microscopy (SMLM) are inconsistent with this traditional view and show that Fn1 fibrils are composed of roughly spherical nanodomains containing 6-11 Fn1 dimers. As they move toward the cell center, Fn1 nanodomains become organized into linear arrays, wherein nanodomains are spaced at the average periodicity of 105±17 nm. Periodical Fn1 nanodomain arrays are bona fide fibrils: they are resistant to deoxycholate treatment and retain nanodomain periodicity in the absence of cells. The nanodomain periodicity in fibrils remained constant when probed with antibodies recognizing distinct Fn1 epitopes or combinations of antibodies recognizing epitopes spanning the length of Fn1. FUD, a bacterial peptide that binds Fn1 N-terminus and disrupts Fn1 fibrillogenesis does not disrupt the formation of Fn1 nanodomains, instead, it blocks the organization of Fn1 nanodomains into periodical arrays. These studies establish a new paradigm of Fn1 fibrillogenesis.

Introduction

Fibronectin (Fn1) is a requisite component of the extracellular matrix (ECM) necessary for embryogenesis and homeostasis (Schwarzbauer and DeSimone, 2011). In the absence of Fn1 fibrillogenesis, the binding of Fn1 to cells is not sufficient to regulate key biological processes such as embryonic development, angiogenesis, vascular remodeling, or cartilage condensation (Chiang et al., 2009; Rozario et al., 2009; Singh and Schwarzbauer, 2014; Zhou et al., 2008). Therefore, understanding the mechanisms by which Fn1 proteins assemble into macromolecular fibrils is essential to gain insights into the various functions of Fn1. Fn1 is secreted as a dimer wherein two Fn1 molecules are held in an anti-parallel orientation by two disulfide bonds close to their C-termini (Skorstengaard et al., 1986; Wagner and Hynes, 1979). Fn1 fibrillogenesis is a cell-dependent process (McKeown-Longo and Mosher, 1983), occurs following the binding of Fn1 dimers to cell-surface integrins (Schwarzbauer and DeSimone, 2011). Following integrin binding, intracellular cytoskeletal forces such as actomyosin contractility acting through integrins generate pulling forces on Fn1 dimers, exposing epitopes that promote Fn1 fibrillogenesis (Chernousov et al., 1987; Hocking et al., 1994; Smith et al., 2007; Zhang et al., 1994; Zhang et al., 1997; Zhong et al., 1998). At a cellular level, the process of Fn1 fibrillogenesis is correlated with the formation of fibrillar adhesions, whereby small mobile adhesions containing Fn1 and integrin $\alpha5\beta1$ somehow elongate while translocating toward the nucleus, first giving rise to focal adhesions (< 1 μm), and then as the translocation continues, to longer filaments, termed fibrillar adhesions ($\geq$1 μm) containing Fn1 and intracellular cytoplasmic effectors linking Fn1 and actin cytoskeleton (Geiger et al., 2001; Geiger and Yamada, 2011; Lu et al., 2020; Pankov et al., 2000; Zamir et al., 1999; Zamir et al., 2000).

It has been thought that Fn1 fibrils resemble ropes, in which extended Fn1 dimers align such that regions containing overlapping N-termini alternate with regions containing C-termini

73 (Chen et al., 1997; Dzamba and Peters, 1991; Fruh et al., 2015), also illustrated in **Sup. Fig.**
74 **8A**. To understand how the process of fibrillogenesis occurs in real-time and at a nanoscale
75 level, we adopted a CRISPR/Cas9-mediated mutagenesis approach to generate fluorescently-
76 labeled Fn1, which was subject to the physiological regulation of expression and splicing. This
77 approach has enabled visualization of Fn1 fibrillogenesis over an extended time. Using live
78 imaging and super-resolution microscopy, we uncovered an unexpected mechanism of Fn1
79 fibrillogenesis.

80 Our data demonstrate that Fn1 fibrils form as a result of centripetally-moving Fn1
81 nanodomains originating at the cell periphery. As Fn1 nanodomains move toward the cell
82 center, they assemble into arrays of periodically-spaced nanodomains. The arrays become
83 longer as the movement towards the cell center continues and as more nanodomains are
84 added. We show that these nanodomain arrays are in bona fide fibrils and that each Fn1
85 nanodomain contains multiple Fn1 dimers. Our live imaging and SMLM reveal a new role by
86 which the N-terminal region of Fn1 protein regulates fibril assembly, and show that interactions
87 mediated by the N-terminal Fn1 assembly region are not required for the formation of Fn1
88 nanodomains or their centripetal translocation; Instead, the N-terminus of Fn1 regulates the
89 organization of Fn1 nanodomains into nanodomain arrays. Our model integrates the process
90 of fibrillogenesis with the process of adhesion elongation and provides significant new insights
91 into the mechanisms of Fn1 ECM formation, remodeling, and signaling.

92

93 **Results**

94 **Beaded structure of Fn1 fibrils revealed by diffraction-limited microscopy**

95 While examining $Fn1^{+}$ ECM in mid-gestation mouse embryos by confocal
96 immunofluorescence microscopy using an Abcam monoclonal anti-Fn1 antibody which binds
97 an epitope within a central region of Fn1 (**Table M2** in Methods), we observed that Fn1 fibrils
98 in the pharyngeal arches and the heart appeared dotted, with regularly-spaced regions of high

99 and low fluorescence intensity (**Fig. 1, Movie 1**). The dotted appearance of embryonic Fn1
100 suggested that the distribution of Fn1 molecules in Fn1 fibrils is not homogenous. To
101 understand how Fn1 fibrils form, we employed a CRISPR/Cas9 knock-in strategy to modify the
102 endogenous Fn1 locus by replacing the termination codon of Fn1 with a sequence encoding a
103 fluorescent protein. We used this strategy to generate cell lines and Fn1$^{mEGFP/mEGFP}$
104 homozygous knock-in mice expressing Fn1 fused to monomeric enhanced green fluorescent
105 protein (mEGFP) or other monomeric fluorescent proteins (**Sup. Figs. 1-2**). Homozygous
106 Fn1$^{mEGFP/mEGFP}$ mice were obtained at the correct Mendelian ratio (**Sup. Fig. 1B,** panels 4 and
107 5), and are viable and fertile, indicating that Fn1-mEGFP supports all functions of Fn1
108 necessary for embryonic development, fetal viability, and adult homeostasis. Examination of
109 Fn1 expression patterns in knock-in mice showed that Fn1-mEGFP is expressed in the same
110 pattern as the unmodified Fn1 in embryos (Peters and Hynes, 1996), i.e., there were no
111 regions that were GFP+ but Fn1-negative and vice versa in Fn1$^{mEGFP/+}$ embryos expressing
112 one wild-type allele of Fn1 (**Sup. Fig. 2D**). In addition, we used CRISPR/Cas9 mutagenesis to
113 generate five independent lines of mouse embryo fibroblasts (MEFs) expressing Fn1-mEGFP,
114 Fn1-mScarlet-I, Fn1-Neon Green, or Fn1-tdTomato fluorescent proteins (FP). Western blots
115 showed that FP fusions to Fn1 were specific: FPs were only fused to Fn1 as no other FP
116 fusions were detected either by western blotting or immunofluorescence (IF) (**Sup. Fig. 2A-B**).
117 Measuring deoxycholate (DOC) insolubility of Fn1 ECM is a classical biochemical assay
118 to assay stable incorporation Fn1 proteins into the ECM (Choi and Hynes, 1979; McKeown-
119 Longo and Mosher, 1983; Schwarzbauer, 1991; Singh et al., 2010; Wierzbicka-Patynowski et
120 al., 2004). For these assays, we carefully controlled the number of cells plated, as cell density
121 affects the extent of Fn1 fibrillogenesis (Hynes, 1990). We performed DOC insolubility assays
122 using 5 independently-generated cells lines expressing Fn1-FP proteins. These experiments
123 demonstrated that the incorporation of Fn1-FPs into the ECM was indistinguishable from wild-
124 type, untagged Fn1 (**Sup. Fig. 2C**). In addition, DOC insolubility assays showed that Fn1-

125 mEGFP proteins isolated from mouse embryos are incorporated into a deoxycholate-insoluble
126 matrix similar to unmodified Fn1 (**Sup. Fig. 2D-E**). Together with the viability of Fn1$^{mEGFP/mEGFP}$
127 homozygous knock-in mice, these data demonstrate that Fn1-FP fusion proteins are suitable
128 reagents for investigating mechanisms of Fn1 fibrillogenesis.

129 To visualize the process of fibrillogenesis in real-time, we plated Fn1$^{mEGFP/+}$ MEFs on
130 the gelatin-coated cover glass and imaged cells 16 hours after plating using total internal
131 reflection (TIRF) microscopy at the critical angle of incidence. These experiments showed that
132 Fn1 fibrillogenesis initiated at cell periphery as distinct, brightly-fluorescent Fn1 densities that
133 moved centripetally in parallel with F-actin and became aligned into linear arrays of "beads"
134 (arrows in **Movie 2**). TIRF imaging also showed that domains of higher fluorescence intensity
135 of Fn1 co-localized with integrin $\alpha5\beta1$ both in non-fibrillar (arrows in **Fig. 2A-A2**) and in fibrillar
136 adhesions (arrows in **Fig. 2B-B2**), and that both Fn1 and $\alpha5\beta1$ fibrillar adhesions appeared
137 beaded (**Fig. 2B-B2**, arrows). Beaded architecture of Fn1 fibrils was also observed by an
138 independent imaging method using Zeiss Airyscan technology (**Sup. Fig. 3**). To test whether
139 the beaded appearance of Fn1 fibrils depended on antibody epitope availability, we stained
140 wild-type MEFs or mouse endothelial cells using three different antibodies 1) 297.1 polyclonal
141 antibody raised against the rat plasma Fn1 protein and recognizing multiple Fn1 epitopes
142 (**Sup. Fig. 4)**; 2) 3E2 monoclonal antibody recognizing the alternatively spliced EIIIA exon of
143 Fn1, and 3) an Abcam monoclonal antibody recognizing an epitope within the central region of
144 Fn1 (see **Table M2**, in Methods). The beaded appearance of Fn1 fibrils did not depend on the
145 type of antibody used (**Sup. Fig. 5**). Moreover, staining with a polyclonal antibody to Fn1,
146 297.1, which recognizes multiple epitopes along the Fn1 molecule resulted in the beaded
147 appearance of Fn1 fibrils (**Sup. Fig. 5A-A1**). Fn1 fibrils formed by cells plated on uncoated
148 glass, as well as on glass coated with gelatin, laminin 111, or vitronectin, also appeared
149 beaded **Sup. Figs. 5-6**). Similarly, Fn1 fibrils in cell-free areas (**Sup. Fig. 5A, A1**) and between

150 cells were beaded (**Sup Fig. 5B, B1, C, C1**). Fn1 fibrils produced by cells plated on soft
151 substrata such as hydrogels of variable stiffness also appeared beaded (**Sup. Fig. 6C-D, 6C1-**
152 **D1**). In this latter experiment, Fn1 was detected by imaging the fluorescence of Fn1-mEGFP
153 protein, indicating that the beaded appearance of Fn1 fibrils is independent of antibody
154 staining. To determine whether Fn1 fibrils in cell-free, fibrillar ECM were beaded, cultures were
155 treated with 2% DOC (Lu et al., 2020). 2% DOC treatment dissolves cell membranes and
156 cytoplasmic components, leaving behind ECM devoid of cell contact (**Movie 3** for time-lapse of
157 dissolution of cellular components, F-actin and DNA). This experiment showed that Fn1 fibrils
158 retained their beaded architecture in the absence of cell contact (**Sup. Fig. 5D**). Taken
159 together, these studies indicated that the beaded appearance of Fn1 fibrils is a general feature
160 of Fn1 ECM that can be seen in multiple contexts: in DOC-resistant cell-free fibrils, in different
161 embryonic tissues *in vivo*, and when cells are cultured on various substrata *in vitro*. Moreover,
162 the beaded appearance of Fn1 fibrils is independent of the type of antibody and a method of
163 detection: It is seen by indirect detection methods such as immunofluorescence and by direct
164 detection of fluorescent Fn1-mEGFP protein.
165

166 **Nanoarchitecture of Fn1 fibrils revealed by standardized single-molecule localization**
167 **microscopy.**

168 To examine the structure of Fn1 fibrils at a nanoscale level, we adopted single-molecule
169 localization microscopy (SMLM) using the direct stochastic optical reconstruction microscopy
170 (dSTORM) method (Heilemann et al., 2008; Rust et al., 2006). To optimize SMLM imaging
171 conditions and determine the effective labeling efficiency of our reagents, we used the
172 methodology and the reference cell line NUP96-mEGFP, as gold-standard tools to optimize
173 image quality, measure effective labeling efficiency, and to quantify the number of GFP
174 molecules in our structure(s) of interest (Lelek et al., 2021; Thevathasan et al., 2019). In this
175 reference cell line, both copies of the *NUP96* gene are modified by CRISPR/Cas9

176 mutagenesis to generate NUP96-mEGFP protein, a component of the nuclear pore complex,
177 NPC (Thevathasan et al., 2019). Thirty-two copies of NUP96 protein are evenly distributed
178 among the eight corners of the NPC at known distances (see schematic in **Sup. Fig. 7**) (Bui et
179 al., 2013; Thevathasan et al., 2019; von Appen et al., 2015). To optimize our SMLM imaging,
180 we were guided by the current best SMLM practices (Lelek et al., 2021; Mund and Ries, 2020),
181 the methodology, and the SMAP software developed by (Diekmann et al., 2020; Ries, 2020;
182 Thevathasan et al., 2019). Measurements using the Fourier ring correlation method
183 (Nieuwenhuizen et al., 2013) implemented in the SMAP software indicated that the resolution
184 of our images ranged between 14 and 28 nm. Localization precision was 9.1±1.9 nm, on
185 average. Using antibodies to detect NUP96-mEGFP and the SMAP software, we analyzed
186 images from 3 independent experiments, 8 nuclei and 4571 NPCs, and determined the NPC
187 radius to be 63.6±0.86 nm (**Fig. 3A-C** and **Table 1**). This radius is consistent with the reported
188 NPC radius of 64.3+/-2.6 nm, measured using this cell line and a combination of commercial
189 anti-GFP primary and Alexa-647-conjugated secondary antibodies (Thevathasan et al., 2019).
190 We then used NUP96-mEGFP cells to optimize the effective labeling efficiency (ELE) of our
191 reagents. ELE summarily measures how well one's reagents and methods, including the
192 SMLM imaging protocol, generate images that reflect the actual structure under the study
193 (Thevathasan et al., 2019). SMLM imaging of NUP96 in the x-y plane should produce 8-fold
194 symmetrical ring-like structures wherein 4 copies of the NUP96 protein are positioned at each
195 of the NPC's 8 vertices at known intervals and with known dimensions (Thevathasan et al.,
196 2019). Using NUP96-mEGFP as a reference cell line, anti-GFP primary antibodies,
197 commercially-labeled Alexa-647-conjugated secondary antibodies, and the SMAP software
198 (Thevathasan et al., 2019), we analyzed 4,571 NPCs from 8 cells and 3 independent
199 experiments, and determined the ELE to be 79.6±5.4% (**Table 1**), reflecting that the majority
200 of NPCs have eight $NUP96^{+}$ corners in our images (**Fig. 3A-C**). This ELE and the standard
201 deviation of our measurements (<10%) are comparable with the best ELE measured for this

202 system ~74% (Thevathasan et al., 2019). Together, these experiments indicate that our
203 reagents and SMLM imaging conditions are within the accepted SMLM standards (Lelek et al.,
204 2021).

205 To attain a comparable ELE to that measured with NUP96-mEGFP, we stained
206 homozygous Fn1$^{mEGFP/mEGFP}$ MEFs at the same time as NUP96-mEGFP cells, using aliquots of
207 the same mixtures of reagents. Furthermore, pairs of stained Fn1$^{mEGFP/mEGFP}$ MEFs and
208 NUP96-mEGFP cells were imaged on the same day, using aliquots of the same imaging
209 buffer, and the same off-switching and imaging protocols (see Methods). Similar to (Fruh et al.,
210 2015), we saw that Fn1 fibrils appeared as arrays of nanodomains situated along Fn1 fibrils
211 with a regular periodicity (**Figs. 3D-F, Fig. 5D-D2, Fig. 6D-D"**). As in (Fruh et al., 2015),
212 nanodomain periodicity was ascertained using autocorrelation, wherein the position of the first
213 autocorrelated peak marks the nanodomain periodicity (see discussion and simulations in
214 (Fruh et al., 2015)). Autocorrelation analysis of 14 fibrils from 7 cells and 3 independent
215 experiments indicated that the nanodomain periodicity of the GFP epitopes in Fn1-mEGFP
216 fibrils was 102±29 nm (**Figs. 6D-D", 6F, Table 2**). This periodicity is comparable to the
217 nanodomain periodicity measured by (Fruh et al., 2015), which was 99±17 nm, and the
218 periodicity determined by immuno-electron microscopy using anti-EIIIA antibody, which was on
219 average 84 nm and ranged between 40 and 280 nm (Dzamba and Peters, 1991).
220

221 **Localization of Fn1 epitopes within periodical nanodomain arrays**

222 Fn1 is a large, multi-domain, ~250 kDa glycoprotein secreted as a dimer, wherein two
223 Fn1 subunits are linked in an anti-parallel orientation by two di-sulfide bonds at their C-termini
224 (**Fig. 4A**), (Schwarzbauer and DeSimone, 2011; Skorstengaard et al., 1986; Wagner and
225 Hynes, 1979). To investigate the relationship between the protein domains of Fn1 and the
226 nanodomain architecture of Fn1 fibrils, we first used antibodies to different regions of Fn1
227 protein (**Figs. 4B** and **Table M2**). For these experiments, Fn1$^{mEGFP/mEGFP}$ MEFs were plated on

228 uncoated glass coverslips. Cells were then fixed and stained with antibodies recognizing
229 different Fn1 epitopes: 1) R457 rabbit polyclonal antibodies raised to the N-terminal 70 kDa
230 domain of Fn1 (Aguirre et al., 1994; Sechler et al., 2001), 2) R184 rabbit polyclonal antibodies
231 raised to recognize the domain immediately following the 70 kDa N-terminal domain and
232 containing the first six type III repeats of Fn1 (Fn1 III_{1-6}) (Raitman et al., 2018), 3) a rabbit
233 monoclonal antibody from Abcam recognizing an epitope within the central region of Fn1
234 (**Table M2** for further description of this antibody), and 4) an anti-GFP antibody recognizing the
235 C-terminus of Fn1-mEGFP protein. In our analyses, we focused on long fibrillar adhesions that
236 were over 1 μm in length, characteristic of mature assembled Fn1 fibrils (Lu et al., 2020).
237 Independent of the antibodies used, Fn1 fibrils appeared as arrays of periodically-
238 spaced nanodomains (**Figs. 5-6**). To ensure that the beaded appearance of fibrils was not due
239 to under-sampling, we tested 2 – 4 dilutions of each antibody, followed by SMLM imaging and
240 autocorrelation analysis, as in (Fruh et al., 2015). Our analyses showed that nanodomain
241 periodicity remained constant at all antibody dilutions tested (**Fig. 5, 6A''-E', summarized in**
242 **6F**). The periodicity of nanodomains detected with either R457, R184, or Abcam monoclonal
243 antibodies was similar to that measured with the anti-GFP antibody, suggesting that each of
244 these antibodies was used at the ELE comparable with that of GFP-labeling reagents. The
245 finding that nanodomain periodicity was independent of antibody specificity supports the
246 conclusion that the beaded appearance of Fn1 fibrils is not a result of a particular Fn1 protein
247 conformation, since staining using antibodies to three different regions of Fn1 in addition to
248 antibodies to GFP resulted in the same pattern. In all cases, nanodomain periodicity was
249 independent of the antibody concentrations, arguing against under-sampling (Fruh et al.,
250 2015).
251 Analysis using DBSCAN (Caetano et al., 2015) discovered clusters corresponding with
252 nanodomains, when the radius of the neighborhood (ε) was set to 14 nm, the average

253 apparent radius of an Fn1 nanodomain (**Table 2**, compare (**Figs. 7A and B**). Unbiased
254 DBSCAN clustering using the neighborhood radius that was automatically estimated by the
255 SMAP software discovered larger clusters of Fn1 nanodomains (**Fig. 7C**). This suggests that
256 Fn1 nanodomains are organized in a higher-order structure within long fibrils, consistent with
257 the observation of "beads" in lower-resolution diffraction-limited images of Fn1 (**Figs. 1, 2** and
258 **Sup. Figs. 3, 5, 6**).
259
260 **Fn1 nanodomains contain multiple full-length Fn1 molecules.**
261 It was previously-thought that Fn1 nanodomains detected by immunoelectron
262 microscopy or by immunofluorescence SMLM corresponded with particular regions in Fn1
263 protein sequence (Dzamba and Peters, 1991; Fruh et al., 2015), illustrated in **Sup. Fig. 8A-B**.
264 Surprisingly, staining using 297.1 polyclonal anti-Fn1 antibody raised against full-length
265 plasma Fn1 and recognizing multiple epitopes along Fn1 protein resulted in the same
266 periodicity of nanodomains as staining with antibodies to distinct regions of Fn1 protein (**Figs.**
267 **6E, 6F, Figs. 8A, 8D**). Since 297.1 polyclonal antibody recognizes multiple epitopes along
268 Fn1, including an epitope in the 70 kDA N-terminal assembly region of Fn1 (**Sup. Fig.4**), these
269 experiments suggested that each Fn1 nanodomains contained at least one entire Fn1 dimer.
270 To determine the number of Fn1 molecules per nanodomain, we used the methodology
271 developed by (Thevathasan et al., 2019), and identical labeling reagents and imaging
272 conditions for the detection of mEGFP in NUP96-mEGFP and Fn1-mEGFP cells (Thevathasan
273 et al., 2019). This analysis indicates that each Fn1 nanodomain contains 16.85 +/- 5.1 mEGFP
274 proteins on average (**Table 2).** Since Fn1 assembled in ECM fibrils is an obligate dimer of two
275 disulfide-bonded Fn1 molecules (Schwarzbauer, 1991), these findings show that Fn1
276 nanodomains contain 6 – 11 Fn1-mEGFP dimers, on average.
277 These results are not consistent with the model that thinnest Fn1 fibrils are made of
278 extended single Fn1 molecules that are periodically aligned in a regular, end-to-end fashion

279 with regions containing N-termini alternating with regions containing C-termini (Chen et al.,
280 1997; Dzamba and Peters, 1991; Fruh et al., 2015) and illustrated in **Sup. Fig. 8A-B**. Such
281 periodic alignment of Fn1 dimers necessitates that staining using antibodies recognizing
282 multiple epitopes along the length of Fn1 molecule would result in a uniform labeling of Fn1
283 fibrils, (**Sup. Fig. 8C**). However, this is not what we observed: staining with a polyclonal 297.1
284 antibody showed that Fn1 fibrils were composed of periodically-spaced nanodomains (**Fig. 8A-**
285 **A", 8D**). Autocorrelation analysis showed that the spacing was periodical at multiple
286 concentrations of 297.1 antibody (**Figs. 6E-E", 6F,** and **8D**). Importantly, the periodicity of
287 nanodomains detected using 297.1 antibody was statistically indistinguishable from
288 periodicities seen with any regions-specific antibody tested, including that of anti-GFP
289 antibodies (**Fig. 6F**). The latter suggested that 297.1 polylconal antibodies were used at an
290 ELE that was at least as high as that for GFP labeling reagents. Finally, the periodical
291 distribution of 297.1 epitopes (average periodicity 121±11) and the presence of multiple Fn1
292 dimers per nanodomain, does not fit with the model proposed by (Dzamba and Peters, 1991),
293 illustrated in **Sup. Fig. 8A**, and suggest a different model of Fn1 fibrillogenesis (e.g., **Fig. 8G**).
294 To further evaluate the hypothesis that Fn1 nanodomains contain full-lengths Fn1
295 dimers, we used combinations of antibodies and the imaging parameters resulting in the high
296 ELE (**Fig. 6F** and Methods). We first stained Fn1$^{mEGFP/mEGFP}$ MEFs using a combination of
297 R457 and anti-GFP antibodies, detecting the N- and C- termini of Fn1-mEGFP, respectively.
298 Consistent with the staining using 297.1 antibody, the periodicity of nanodomains detected with
299 a mixture of R457 and anti-GFP antibodies was 101±45 nm, which is statistically
300 indistinguishable from the periodicities when either of these antibodies were used alone (**Figs.**
301 **6F, 8B-B", 8E**).
302 Next, we stained Fn1$^{mEGFP/mEGFP}$ MEFs with a cocktail of five antibodies recognizing
303 epitopes distributed along the length of the Fn1 molecule: 1) the N-terminal 70 kDa assembly
304 domain of Fn1 (R457), 2) the sequence immediately following the 70 kDA domain (R184), 3)

305 an epitope in the middle of Fn1 (Abcam monoclonal), 4) multiple epitopes along the Fn1
306 protein (297.1), and 5) the anti-GFP antibody marking the C-terminus of Fn1-mEGFP (αGFP)
307 **(Fig. 8C-C", 8F**). Each antibody was used at a dilution resulting in a periodical staining (**Fig.**
308 **6F** and legend). The binding of all primary antibodies in the cocktail was detected by a cocktail
309 of Alexa 647-conjugated secondary antibodies. If Fn1 fibrils were indeed composed of
310 continuous, linear arrays of extended and periodically aligned Fn1 molecules, this cocktail of
311 antibodies recognizing epitopes from the N- to the C-termini of Fn1 would uniformly label Fn1
312 fibrils. Even in the scenario in which R457 epitopes did not extend to the N-terminal-most
313 sequence of Fn1, the staining using this mixture of five antibodies would not be expected to
314 produce periodical staining. However, we observed that the cocktail of 5 antibodies labeled
315 nanodomains with the average periodicity of 94±47 nm at the spatial resolution of 23 nm in thin
316 Fn1 fibrils (**Fig. 8C-8C", 8F**). This periodicity was statistically indistinguishable from the
317 periodicities of individual antibodies at all the dilutions tested (**Fig. 6F**).
318 Unbiased clustering using the Voronoi tessellation method (Andronov et al., 2016b)
319 implemented in SMAP showed that Fn1 fibrils stained with the 5-antibody cocktail can be
320 segmented into clusters (**Fig. 8C", 8C"-1**). This analysis shows that the nanodomain structure
321 of Fn1 fibrils can be discovered using an unbiased computational approach. The size of the
322 nanodomains detected with the 5-antibody cocktail was larger than when nanodomains were
323 detected by the use of any single antibody (e.g., compare **Fig. 8A"** with **Fig. 8C"**). This type of
324 behavior is expected in SMLM when molecules are clustered (Baumgart et al., 2016).
325 In agreement with the results described above, periodically-spaced nanodomains were
326 detected in Fn1 fibrils using two other cell lines, heterozygous $Fn1^{mEGFP/+}$ MEFs and wild-type
327 MEFs (**Sup. Fig. 9**). The presence of the periodical nanodomains in fibrils produced by wild-
328 type cells indicates that the periodical structure of Fn1 fibrils is not an artifact of GFP labeling.
329 Nanodomain spacing in Fn1 fibrils treated with 2% DOC, which removes cells and cellular

330 components, was similar to that of untreated fibrils (**Sup. Fig. 9,** columns **4** and **8,** and **Sup.**
331 **Fig. 9F**). Together, these data indicate that the nanodomain architecture of Fn1 fibrils is
332 independent of antibody(ies) used for staining, is seen in cells expressing wild-type Fn1 and in
333 the absence of cell contact, and that periodically-spaced nanodomains within Fn1 fibrils
334 contain multiple Fn1 dimers (e.g., model in **Fig. 8G**).

335 To further test the hypothesis that Fn1 nanodomains contain full-length Fn1 molecules,
336 we performed double-color dSTORM experiments, wherein the N-terminus of Fn1 was labeled
337 with the R457 primary antibody and anti-rabbit CF680-conjugated secondary immunoglobulins,
338 and the C-terminus of Fn1-mEGFP was labeled with the anti-GFP primary antibody and Alexa-
339 647-conjugated anti-chicken secondary antibodies. As a control, we stained $Fn1^{mEGFP/mEGFP}$
340 MEFs using two different anti-GFP antibodies, one made in rabbit (detected using CF680-
341 conjugated secondary antibodies) and the other, in chicken (detected with Alexa-647-
342 conjugated anti-chicken secondary antibodies). The majority of nanodomains detected using
343 the two anti-GFP antibodies contained overlapping CF680 and AF647 localizations, suggesting
344 a high ELE for both reagents (**Fig. 9A-C,C'**; Gray lines in **Fig. 9A', 9B'** mark overlapping
345 staining in nanodomains). Nanodomains in which the two labels did not overlap were marked
346 by purple lines (**Fig. 9A', 9B'**). To determine the extent of co-localization between the two
347 labels, we performed coordinate-based colocalization (CBC) analysis, a widely-accepted
348 method for detecting co-localization in SMLM data (Malkusch et al., 2012). The CBC
349 coefficient was calculated by counting the number of CF680 localizations within a radius *r* of
350 each of the AF647 localizations and normalizing by the number of localizations within the area
351 πR^2_{max} (Malkusch et al., 2012) (**Fig. 9D,F**). Conversely, we also determined the CBC coefficient
352 by counting the number of AF647 localizations within a radius *r* of each of the CF680
353 localizations and normalizing by the number of localizations within the area πR^2_{max} (**Fig. 9E,F**).
354 The CBC coefficients were calculated using algorithms implemented either by the Abbelight

355 software or by the publicly-available ThunderSTORM software (Ovesny et al., 2014). The
356 coefficient "+1" indicates a high probability of co-localization, while CBC ≤ 0 indicates low
357 probability of co-localization. CBC analysis using the Abbelight software and color-coding
358 according to the CBC coefficient, showed that the parameters chosen for these analyses,
359 r=30nm and R_{max}=300nm, reflect the overlap (e.g., yellow color in **Fig. 9D-E** and gray lines in
360 **Fig. 9A'-B'**) and the lack of overlap (purple color and arrows in **Fig. 9D-E** and purple lines and
361 arrows in **Fig. 9A'-B'**) seen in SMLM images. These figures also show that we can detect non-
362 overlapping signals in nanodomains located next to one another (**Fig. 9D-F**). CBC analyses
363 performed on twenty-two regions containing long (≥1μm) Fn1 fibrils from $Fn1^{mEGFP/mEGFP}$ MEFs
364 showed extensive overlap among localizations arising from rabbit and chicken anti-GFP
365 antibodies (**Fig. 9F**).
366 CBC analyses of twenty regions containing long fibrils from $Fn1^{mEGFP/mEGFP}$ MEFs
367 stained with R457 and anti-GFP antibodies showed extensive overlap between R457 and anti-
368 GFP localizations, detecting the N- and the C- termini of Fn1-mEGFP, respectively (**Fig. 9G-**
369 **L**). Using ThunderSTORM software, we varied the parameters of CBC analysis, e.g., setting
370 the radius r from 2 or 5 nm and R_{max} from 20 or 50nm, respectively. These analyses had the
371 same outcome as above, i.e., CBC coefficients were close to +1, indicating a high probability
372 of overlap among localizations resulting from R457 and anti-GFP antibody binding (**Sup. Fig.**
373 **10**). Together, these studies show that the N- and the C-termini of Fn1 are contained within
374 each Fn1 nanodomain and support the model wherein Fn1 nanodomains in Fn1 fibrils contain
375 multiple full-length Fn1 molecules (**Fig. 8G**).
376
377 **Nanoarchitecture of Fn1 fibrils formed by ectopically-added Fn1**
378 It is known that ectopic Fn1 added to cells becomes assembled into fibrils (McKeown-
379 Longo and Mosher, 1983). To determine whether fibrils incorporating ectopically-added Fn1

380 contain nanodomains, we first used live imaging to film the assembly of ectopic Fn1. In these
381 experiments, MEFs producing Fn1-mEGFP were cultured on the uncoated glass inside an
382 insert while a confluent monolayer of MEFs producing Fn1-tdTomato was grown in the space
383 surrounding the insert. Prior to imaging, the insert was lifted, and Fn1-mEGFP+ MEFs were
384 imaged at ~17 min intervals for 16 hours. These movies show that Fn1-tdTomato fibrils
385 become clearly visible on the surface of Fn1-mEGFP cells by about 3 hours of co-culture
386 without first accumulating inside cells, suggesting that ectopic Fn1 is assembled into fibrils at
387 the cell surface (**Movie 4**). To determine the nanoarchitecture of Fn1 fibrils formed by
388 ectopically-added Fn1, we cultured $Fn1^{mEGFP/mEGFP}$ MEFs in the presence of 10 μg of Fn1-
389 tdTomato for 24 hours. Cells were fixed and stained without permeabilization using rabbit anti-
390 Cherry primary antibodies and anti-rabbit Alexa647-conjugated secondary antibodies. ECM in
391 regions between cells was imaged using TIRF to detect Fn1-mEGFP and Fn1-tdTomato
392 fluorescence, and dSTORM to detect Fn1-tdTomato due to the Alexa 647 label. Fn1-tdTomato
393 extensively co-assembled with Fn1-mEGFP (**Sup. Fig. 11A-B**), and high-resolution SMLM
394 reconstructions of thin and thick fibrils contained nanodomain arrays composed of Fn1-
395 tdTomato proteins (**Sup. Fig. 11C-E, 11F)**. Together, these experiments demonstrate that 1)
396 Fn1 fibrils deposited into the intercellular ECM space are composed of nanodomain arrays and
397 2) ectopic Fn1 assembles into fibrils comprised of nanodomain arrays.
398

399 **Fibrillogenesis inhibitor FUD disrupts the organization of Fn1 nanodomains into**
400 **periodical arrays**

401 To understand the relationship between the nanodomain architecture of Fn1 fibrils and
402 the process of fibrillogenesis, we adopted a live imaging approach using $Fn1^{mEGFP/+}$ MEFs and
403 inhibitors of fibrillogenesis. One such inhibitor is a 49-amino acid peptide derived from
404 *Streptococcus pyogenes* adhesin F1, termed the functional upstream domain (FUD), a highly

405 potent inhibitor of Fn1 fibrillogenesis (Tomasini-Johansson et al., 2001). Fn1 fibrillogenesis
406 critically depends on the interactions mediated by the N-terminal 70 kDa assembly domain of
407 Fn1 (**Fig. 4A**), and FUD is one of the inhibitors that interferes with these interactions (Filla et
408 al., 2017; Morla et al., 1994; Schwarzbauer, 1991; Sechler et al., 2001; Sechler et al., 1996;
409 Tomasini-Johansson et al., 2001).

410 To further investigate the mechanism of Fn1 fibrillogenesis and the role of the N-
411 terminal domain of Fn1 in this process, Fn1$^{mEGFP/+}$ MEFs were plated on uncoated glass for 4
412 hours, and then imaged for 15 – 18 hours either in the imaging medium alone, or in the
413 medium containing 225 nM FUD. We also imaged cells incubated with 274 nM 11-IIIC peptide,
414 a 68 amino-acid control peptide that does not interfere with Fn1 fibrillogenesis (Morla et al.,
415 1994; Sottile and Chandler, 2005). Untreated cells or cells treated with the control peptide
416 developed and accumulated long Fn1 fibrils (**Movie 5**). In contrast, treatment with FUD led to
417 a) the dismantling of the pre-existing Fn1 fibrils and b) inhibiting the formation of new Fn1
418 fibrils (**Movie 6)**. Instead of fibrils, cells cultured in the presence of FUD mainly contained
419 centripetally-moving Fn1-mEGFP fluorescent "beads" that only rarely assembled into fibrils
420 (**Movie 6**). These experiments suggested that FUD inhibits fibrillogenesis by interfering with
421 the process by which Fn1 "beads" become arranged or connected into linear arrays. To test
422 this hypothesis, Fn1$^{mEGFP/+}$ MEFs were plated for 16 hours in the continuous presence of either
423 225 nM FUD or 274 nM III-11C control peptides or were left untreated. Cells were then washed
424 with PBS, fixed, and stained without permeabilization using monoclonal anti-Fn1 antibodies
425 and Alexa Fluor 647-conjugated secondary antibodies, and imaged at the critical angle of
426 incidence by STORM (Jimenez et al., 2020). This approach maximizes the detection of cell-
427 surface Fn1 due to: a) the absence of a detergent during fixation, staining and washing and b)
428 imaging at the critical angle of incidence to detect fluorescence in close proximity to the
429 plasma membrane. These experiments demonstrated that the organization of Fn1
430 nanodomains into linear arrays was lost upon incubation with FUD (compare **Fig. 10A, B, A1,**

431 **B1** with **Fig. 10C, C1**). Non-fibrillar (NF) Fn1 nanodomains in cells treated with FUD had a
432 similar number of Fn1 localizations per nanodomain, and were of similar sizes compared with
433 fibrillar or non-fibrillar Fn1 nanodomains in untreated cells, or cells incubated with the control
434 peptide (**Fig. 10A2, 10B2, 10C2**, **10D**). Taken together, these data indicate that FUD does not
435 interfere with the formation of Fn1 nanodomains but inhibits the organization of Fn1
436 nanodomains into linear arrays. Since Fn1 proteins lacking the N-terminal assembly domain do
437 not form fibrils (Schwarzbauer, 1991), our experiments suggest that interactions mediated by
438 the N-terminal assembly domain of Fn1 with a yet unidentified factor(s), are critical for the
439 organization of Fn1 nanodomains into fibrillar arrays (**Fig. 10E** and *vide infra*).
440

441 **Discussion**

442 In this manuscript, we describe data supporting a novel mechanism underlying the process of
443 Fn1 fibrillogenesis. In this model, 6-11 Fn1 dimers assemble into nanodomains containing
444 integrin $\alpha5\beta1$ at the cell periphery, move rearward with actin flow, and become organized into
445 linear arrays of periodically-spaced nanodomains. Joining of the additional Fn1 nanodomains
446 to these arrays leads to the generation of longer and longer fibrils as nanodomain assemblies
447 move toward the cell center. We show that these periodical nanodomain assemblies are bona
448 fide Fn1 fibrils.

449 The N-terminus of Fn1 is essential for Fn1 fibrillogenesis (Schwarzbauer, 1991). FUD
450 binds tightly to the N-terminal domain of Fn1 (K_D<2.6 nM), with a fast k_{on} and a slow k_{off}, and
451 acts as a competitive inhibitor of Fn1-Fn1 interactions (Ma et al., 2015; Maurer et al., 2010;
452 Tomasini-Johansson et al., 2001). Although in the absence of FUD, individual fibrils in an
453 established matrix are stable and can be tracked for over 16 hours (S.A., unpublished
454 observations), when FUD is added to cells, it localizes with Fn1 fibrils and dismantles the
455 mature Fn1 ECM (Filla et al., 2017; Tomasini-Johansson et al., 2001). These findings suggest

456 that the fibrillar Fn1^{+} ECM is maintained through dynamic interactions mediated by the 70 kDa
457 Fn1 N-terminal domain. Our live imaging experiments demonstrated that in addition to
458 dismantling pre-existing fibrils, FUD effectively blocks their de-novo formation. SMLM showed
459 that FUD does not affect the formation of Fn1 nanodomains, instead, it blocks the organization
460 of Fn1 nanodomains into linear arrays. Together, these data suggest that FUD blocks the
461 dynamic interactions between the N-terminal Fn1 assembly domain and factor(s) linking Fn1
462 nanodomains into fibrils. One of the factors spanning the nanodomains could be an extended
463 Fn1 dimer because we have observed occasional localizations of Fn1 molecules between
464 nanodomains (e.g., **Figs. 6D** or **8A"**). Rare Fn1 localizations seen between Fn1 nanodomains
465 are likely derived from cellular Fn1 as opposed to plasma Fn1 found in the fetal bovine serum
466 in the complete medium (Table M1 in Methods). This is because bovine Fn1 in the complete
467 medium, albeit recognizable by the 297.1 polyclonal antibodies (**Sup. Fig. 12B**), is not
468 incorporated into Fn1 fibrils at a detectable level (**Sup. Fig. 12A**).
469 Previously, the periodical distribution of domain-specific antibody epitopes in EM and
470 SMLM images of Fn1 fibrils was explained by a model stipulating that Fn1 fibrils are made of
471 aligned and extended Fn1 molecules (Dzamba and Peters, 1991) (**Sup. Fig. 8A-B**). In EM
472 micrographs of Fn1 molecules sprayed onto mica surface, one can see extended Fn1 dimers
473 that are on average 120-140 nm in length (Engel et al., 1981; Erickson et al., 1981). Therefore,
474 it was hypothesized that spacing of ~84 nm seen in EM with domain-specific antibodies
475 (Dzamba and Peters, 1991) or spacing of ~100 nm in SMLM images (Fruh et al., 2015) was
476 due to the overlap between the extended Fn1 molecules at their N-termini (Dzamba and
477 Peters, 1991), e.g., (**Sup. Fig. 8B,** overlap marked by a bubble). The findings that the N-
478 terminal 70 kDa domain is required for Fn1 fibrillogenesis, that this domain can mediate
479 intermolecular Fn1-Fn1 interactions, and that inhibitors of Fn1 fibrillogenesis bind to this
480 domain were interpreted in favor of this model. However, these biochemical data are also

481 consistent with a very different model of Fn1 fibrillogenesis (**Sup. Fig. 8**), one that was
482 proposed by (Tomasini-Johansson et al., 2006) and discussed below.
483 A canonical model poses that Fn1 fibrillogenesis entails intermolecular Fn1-Fn1
484 interactions mediated by the 70 kDa N-terminal domain of Fn1 (Hocking et al., 1994; Zhong et
485 al., 1998), summarized in (Singh et al., 2010). These interactions were hypothesized to be
486 important for linking extended and periodically-aligned Fn1 dimers into fibrils (e.g., **Sup. Fig.**
487 **8A**). It was stipulated that FUD blocks Fn1 fibrillogenesis because of its ability to compete with
488 Fn1-Fn1 intermolecular interactions and disassemble fibrils by inhibiting intermolecular
489 interactions between Fn1 dimers (**Sup. Fig. 8D**).
490 However, these biochemical and cell biological experiments are also consistent with a
491 different model, wherein Fn1 fibrillogenesis is mediated by the binding of the 70 kDa N-
492 terminal domain to as of yet an unidentified factor(s). Examples of such factors could be tissue
493 transglutaminase-2 (Akimov et al., 2000; Yuan et al., 2007) or large apparent molecular mass
494 cell-surface complexes (LAMMs) (Tomasini-Johansson et al., 2006; Zhang and Mosher, 1996)
495 (**Sup. Fig. 8E**). Thus, as an example, FUD can disrupt fibrillogenesis by disrupting the
496 interactions between the 70 kDa Fn1 assembly domain and LAMMs (**Sup. Fig. 8E**).
497 Biochemical evidence supporting this model is multifold: 1) isolated 70 kDa N-terminal domain
498 can bind to Fn1-null cells in the absence of Fn1, forming short linear arrays; this binding is
499 time- and dose-dependent, and is detectable with as little as 5 nM of 70 kDa N-terminal
500 segment of Fn1 (Tomasini-Johansson et al., 2006); 2) Incubation of the 70 kDa domain of Fn1
501 with cells precipitates LAMMs in pull-down assays (Zhang and Mosher, 1996); 3) LAMMs
502 contain trypsin-sensitive protein(s) (Zhang and Mosher, 1996); and 4) FUD inhibits the binding
503 of 70 kDa N-terminal fragment to Fn1-null cells (Tomasini-Johansson et al., 2006). These
504 findings suggest that Fn1 nanodomains in fibrils can be held together by the interactions
505 between the 70 kDa N-terminal assembly domain of Fn1 and LAMMs (**Sup. Fig. 8F1**).
506 However, at this time, we cannot rule out the possibility that Fn1 nanodomains are held by an

507 extended Fn1 molecule via N-N-terminal interactions (**Sup. Fig. 8F2**), or that a combination of
508 the latter two models may be true.

509 Our model in which Fn1 fibrils are composed of periodically-spaced nanodomains
510 containing multiple Fn1 dimers is also supported by electron microscopy and atomic force
511 microscopy studies done in the past: 1) periodical staining of Fn1 fibrils was observed in EM
512 with polyclonal antibodies raised to entire human plasma Fn1 (Furcht et al., 1980a); 2) grapes-
513 on-a-vine appearance of immuno-gold complexes detecting plasma Fn1 in fibrils in electron
514 micrographs (Peters et al., 1990); 3) bulbous appearance of Fn1 fibrils in cryo-scanning
515 transmission electron tomography images (Lansky et al., 2019); and 4) beaded appearance of
516 Fn1 fibrils detected by atomic force microscopy (Gudzenko and Franz, 2015). The latter two
517 methods did not rely on antibody staining to detect Fn1 nanodomains, supporting the notion
518 that the beaded architecture of Fn1 fibrils is not an artifact of antibody labeling.

519 Together with our data, these experiments suggest a new model of Fn1 fibrillogenesis
520 (**Fig. 10E**). In this model, Fn1 nanodomains containing multiple Fn1 dimers form at cell
521 periphery. These nanodomains may be similar to focal complexes or adhesion-related particles
522 seen by cryo-electron tomography by (Patla et al., 2010). The centripetal translocation of Fn1
523 nanodomains is coordinated with their organization into linear arrays, giving rise to focal
524 adhesions composed of ~3-5 Fn1 nanodomains and long Fn1 fibrillar adhesions composed of
525 dozens of nanodomains. Fn1 fibrils generated in this process are then incorporated into Fn1
526 ECM (Mautner and Hynes, 1977; Pankov et al., 2019; Sivakumar et al., 2006). Two pieces of
527 evidence suggest that Fn1 nanodomains in fibrils are linked: 1) the preservation of the linear
528 organization and the nanoarchitecture of Fn1 fibrils after the treatment of cells with DOC which
529 dissolves cell membranes, and 2) the presence of fibrous material between immunogold
530 densities in electron micrographs (Chen et al., 1997; Dzamba and Peters, 1991; Furcht et al.,
531 1980a; Furcht et al., 1980b; Furcht et al., 1980c; Lansky et al., 2019; Peters et al., 1990). The
532 sparsity of Fn1 localizations between Fn1 nanodomains in fibrils suggests that molecules other

533 than or in addition to Fn1 participate in the potential linking of Fn1 nanodomains into periodical
534 nanodomain arrays.

535 The beaded architecture of Fn1 ECM has important implications for the mechanisms of
536 ECM formation, remodeling, and signal transduction. The tensile strength of knotted strings is
537 significantly lower than that of strings with uniformly-aligned fibers (Arai et al., 1999; Saitta et
538 al., 1999), thus the beaded architecture of Fn1 fibrils may facilitate their rupture under strain
539 (Ohashi et al., 1999). The non-uniform, nanodomain architecture of Fn1 may facilitate the
540 accessibility of Fn1 fibrils to matrix metalloproteases. In this model, degradation of Fn1 fibrils
541 by metalloproteases may be accomplished by the cleavage of LAMMs between Fn1
542 nanodomains facilitating dynamic ECM remodeling. Finally, Fn1 is known to bind growth
543 factors (Martino and Hubbell, 2010; Saunders and Schwarzbauer, 2019; Wijelath et al., 2002),
544 and cell adhesion to ECM is known to orchestrate growth factor signaling (Hynes, 2009). Thus,
545 Fn1 nanodomains could serve as platforms for the binding and presentation of concentrated
546 packets of growth factors to cells, the organization of Fn1 nanodomains into closely-spaced
547 arrays could further facilitate clustering and signaling by growth factor receptors.
548

549 **Acknowledgments**

550 We thank Richard Hynes and Nathan Astrof for insightful discussions and careful reading of
551 the manuscript, Sydney Astrof for encouragement and help with data entry, Patrick Murphy for
552 endothelial cells, Richard Hynes for the gift of 297.1 antibody, Tung Chan for help with setting
553 up Western Blotting using ProteinSimple, and Jonas Ries for advice that helped us improve
554 SMLM resolution of our imaging, and for his help with adopting the SMAP software. Epitope
555 mapping of 297.1 antibody was performed by PEPperPRINT GmbH, Heidelberg, Germany.
556

557 **Sources of Funding** This work was supported by the funding from the National Heart, Lung,
558 and Blood Institute of the NIH R01 HL103920, R01 HL134935, R01 HL158049, American

559 Heart Association Transformative Project Award 20TPA35490074 to SA, and by the NIH Office
560 of the Director R21 OD025323-01 to SA, by the pre-doctoral fellowship F31HL151046 to BEA,
561 by the National Institute of General Medicine R35GM122505 to AK, by the National Institute of
562 Arthritis and Musculoskeletal and Skin Diseases R01 AR073236 to JES, by the Faculty Seed
563 Grant from the Center for Engineering MechanoBiology (CEMB), an NSF Science and
564 Technology Center, under grant agreement CMMI: 15-48571. Any opinions, findings, and
565 conclusions or recommendations expressed in this material are those of the authors and do
566 not necessarily reflect the views of the National Science Foundation. The authors declare no
567 competing financial interests

568

569 **Materials and Methods**

570 **Generation Fn1-fluorescent protein targeting constructs** Sequences of monomeric (m)
571 green fluorescent protein (GFP), mNeonGreen, mScarlet-I, and tdTomato were obtained from
572 FPbase (https://www.fpbase.org). The sequence encoding one of the above fluorescent
573 proteins (FPs) was knocked into the Fn1 locus following the last coding exon of mouse Fn1,
574 and separated from the last coding amino acid by a flexible, proline-rich linker, PPPELLGGP
575 (Snitkovsky and Young, 1998). Targeting was achieved by CRISPR/Cas9 (Ran et al., 2013).
576 The sequence of the guide RNA was chosen and off-target sites were identified using
577 GuideScan and Off-Spotter software (Perez et al., 2017; Pliatsika and Rigoutsos, 2015). The
578 guide RNA (gRNA) sequence 5'-AGC GGC ATG AAG CAC TCA AT-3' targeting the last
579 coding exon of *Fn1* was subcloned downstream the U6 promoter into the PX459 vector
580 (Addgene, cat # 62988) encoding the Cas9-2A-Puromycin cassette (Ran et al., 2013). The
581 homology-directed repair (HDR) template was constructed using pBS-KS vector (Sup. Fig. 1a).
582 The sequence of the last coding exon of *Fn1* 5'-
583 AACGTAAATTGCCCCATTGAGTGCTTCATGCCGCTAGATGTGCAAGCTGACAGAGACGAT

584 TCTCGAGAG-3' was modified to 5'-

585 AACGTAAATTGCCCCATcGAaTGCTTCATGCCGCTAGATGTGCAAGCTGACAGAGACGATT

586 CTCGAGAG-3' in the HDR template by introducing silent mutations (underlined) to prevent

587 targeting of the template by the gRNA. Homology arm 1 contained 677 bp encoding exon #45,

588 intron, and a portion of the last exon (#46), of the transcript *ENSMUST00000055226.12*.

589 Homology arm 2 encoded 1739 bp immediately downstream of the *Fn1* termination codon and

590 included the unmodified 3'UTR of Fn1. Knockin Fn1$^{mEGFP/+}$ mice were generated by

591 Biocytogen using the same HDR construct and a longer gRNA, 5'-TAG CGG CAT GAA GCA

592 CTC AAT GG-3',

593 targeting the same sequence in the last coding exon (differences between the two gRNAs are

594 underlined). Targeting was confirmed by sequencing and Southern Blotting

595 (Sub. Fig. 1b). 500 bp around each of the top ten predicted off-target sites were sequenced

596 and no mutations were found in the founder mice. Mice containing correctly-targeted *Fn1* locus

597 were used to establish living colonies of Fn1$^{mEGFP/mEGFP}$ animals. Wild-type, Fn1$^{mEGFP/+}$, and

598 Fn1$^{mEGFP/mEGFP}$ mice were genotyped using the following primers Fn1-WT-Fwd 5'-

599 TCCCCGAAACACACACACTTTTGGT-3', Fn1-WT-Rev 5'

600 GTCACCCTGTTCTGCTTCAGGGTTT-3', and Fn1GFP-Rev 5'-

601 GACCCGCGCCGAGGTGAAG-3'. Wild type band is Fn1-WT-Fwd and Fn1-WT-Rev give rise

602 to 372 bp for the wild-type allele; Fn1-WT-Fwd and Fn1GFP-Rev primer located in the GFP

603 sequence give rise to 512 bp if the targeted allele is present. Mice were housed in an

604 AAALAC-approved barrier facility. All experimental procedures were approved by the

605 Institutional Animal Care and Use Committee of Rutgers University and conducted in

606 accordance with the Federal guidelines for the humane care of animals.

607

608 **Cell Culture**

609 **Table M1. Media**

	Cells	Composition of Medium
Complete medium	MEFs	High-glucose Dulbecco's Modified Eagle Medium (DMEM, Corning, cat # 10-013-CV) supplemented with 10% v/v fetal bovine serum (Gemini Biosciences, cat # 100-106), 1% v/v penicillin/streptomycin solution (GE Healthcare, cat #SV30010), 1% v/v L-glutamine (Gibco, cat # 35050-061).
Imaging medium	MEFs	FluoroBrite DMEM (Thermo Fisher Scientific, catalog # A1896701) supplemented with 2% v/v fetal bovine serum (Gemini Biosciences 100-106), 1% v/v penicillin/streptomycin solution (GE Healthcare, SV30010), 1% v/v L-glutamine (Gibco 35050-061), pH8.14.
McCoy's 5a	Nup96-mEGFP U2OS cells	McCoy's 5a medium containing 1xGlutaMax (ThermoFisher, cat #35050061), 10% v/v fetal bovine serum (Gemini Biosciences, cat # 100-106), and 1x penicillin/streptomycin (GE Healthcare, cat #SV30010).

610

611 **Cells** Wild-type mouse embryonic fibroblasts (MEFs) were isolated from embryonic day (E)
612 13.5 embryos derived from the C57BL/6J strain (Jackson Labs, stock # 664) according to
613 established protocols (Behringer et al., 2014) and cultured in complete medium. For
614 propagation, MEFs were plated in flasks pre-coated with 0.1% gelatin solution and grown in
615 complete medium at 37°C, 5% CO_2.

616 $Fn1^{flox/+}$;$Rosa^{mTmG/+}$ MEFs were isolated from E13.5 embryos, as above, and express
617 membrane-bound tdTomato and wild-type Fn1 in the absence of Cre recombinase (Muzumdar
618 et al., 2007). Fn1-null MEFs were generated by treating $Fn1^{flox/-}$;$Rosa^{mTmG/+}$ cells with Ad-Cre-

619 IRED-GFP virus according to the manufacturer's recommendations (Vector Biolabs, #1710). In
620 this experiment, Cre-recombinase is expressed transiently and mediates site-specific
621 recombination between a pair of loxP sites flanking the 1st exon of Fn1 (Sakai et al., 2001) and
622 another pair of loxP sites flanking the STOP cassette in the mTmG reporter (Muzumdar et al.,
623 2007). Three days following infection with Ad-Cre-IRED-GFP, GFP+ cells were sorted resulting
624 in a pure population of Fn1-null MEFs (confirmed by Western Blotting, data not shown, and
625 immunofluorescence, **Sup. Fig. 12**). Fn-null MEFs were culture on gelatin-coated dishes in
626 complete medium.

627 Fn1-FP cells (except Fn1-mEGFP cells) were generated by CRISPR/Cas9 mutagenesis
628 of wild-type MEFs. CRISPR/Cas9 targeting was performed by transfecting wild-type MEFs
629 using the PX459 plasmid encoding Fn1 gRNA and the HDR template using lipofectamine
630 3000, as described (Ran et al., 2013). MEFs expressing Fn1-mEGFP proteins used for live
631 imaging and STORM were generated from homozygous E13.5 Fn1$^{mEGFP/mEGFP}$ or, when noted
632 from Fn1$^{mEGFP/+}$ embryos. Fn1$^{mEGFP/mEGFP}$ MEFs were used to quantify Fn1 molecule number in
633 nanodomains, measure nanodomain spacing, and nanodomain diameter, as well as in
634 experiments to label both the N- and the C-termini of Fn1. For live imaging, Fn1$^{mEGFP/+}$ were
635 used. Fibronectins from Fn1$^{mEGFP/mEGFP}$ and Fn1$^{mEGFP/+}$ cells behave equivalently in Fn1 matrix
636 assembly assays (data not shown).

637 Nup96-mEGFP cells ((Thevathasan et al., 2019), clone #195, Cell Line Services, CLS,
638 clsgmbh.de, catalogue no. 300174)) were cultured according to the vendor's specifications in
639 McCoy's 5a medium containing 1xGlutaMax (ThermoFisher, cat #35050061), 10% v/v fetal
640 bovine serum (Gemini Biosciences, cat # 100-106), and 1x penicillin/streptomycin (GE
641 Healthcare, cat #SV30010).

642

643 **Reagents and buffers**

644 FUD and III-11C peptides were generated as described (Sottile and Chandler, 2005; Tomasini-
645 Johansson et al., 2001) and stored in PBS at -80° C. 4% DOC solution was prepared by
646 dissolving 0.4 g deoxycholate salt (Sigma, catalog # D6750) in 10 ml of imaging medium; the
647 solution was then vortexed and filter sterilized. The pH of the final solution was 8.01. 16%
648 paraformaldehyde (PFA) (Electron microscopy Sciences; catalog # 50-980-487) was diluted in
649 1x PBS to prepare 4% PFA. The 4% PFA solution was aliquoted into 1 ml microfuge tubes,
650 stored at -80° C, and thawed at 37° C immediately before use.
651
652 1X phosphate buffered saline pH 7.5 (PBS) was prepared from 10X PBS (VWR, catalog #
653 76180-740). PBST was prepared using Triton X-100 (Sigma-Aldrich, catalog # T-8787) and
654 contained 0.1% Triton for all stainings except those involving Nup96-mGEFP cells, as detailed
655 below. Blocking buffer was prepared by adding 10% Donkey serum (Sigma-Aldrich, catalog #
656 D9663) to 1X PBST; 5 mg/ml stock of DAPI (Fisher Scientific, cat #D3571) was prepared in
657 water and used at 1:300 dilution. Stain Buffer (cat # 554656 BD Pharmingen) was used for
658 antibody dilutions and washing of cells that were stained without permeabilization.
659 Hoechst 33342 Trihydrochloride (Thermo Fisher, catalog # H1399, 10mg/ml) was used for
660 labelling live MEFs at 1:300 dilution. In live MEFs, F-actin was labelled using SiR actin (cat#
661 CY-SC001 used at 1 μM final concentration). mCardinal-Lifeact-7 was a gift from Michael
662 Davidson (Addgene plasmid # 54663 ; http://n2t.net/addgene:54663 ; RRID:Addgene_54663).
663 Vectashield antifade mounting medium (Vectorlabs, catalog # H-1000) was used for cover
664 slipping.

665 For STORM imaging, we used 25 mm high precision glass cover slips #1.5H (Marienfeld ref#
666 0117650, obtained from Azer Scientific, PA, USA, cat # ES0117650) without coating. Prior to
667 their use, glass cover slips were cleaned using concentrated nitric acid, washed in water, air

668 dried, and autoclaved, as described in (Kaech and Banker, 2006). Clean coverslips were
669 stored in sealed 6-well plates for no longer than a week prior to their use.

670 GLOX/BME STORM buffer contained 50 mM Tris-HCl (Fisher Scientific, catalog # T-395-1),
671 pH 8.0, 10 mM NaCl (Sigma- Aldrich, catalog # S-7653), 10% glucose (Sigma- Aldrich, catalog
672 # G8270), 0.5 mg/ml glucose oxidase (Sigma- Aldrich, catalog # G2133), 40 μg/ml catalase
673 (Sigma- Aldrich, catalog # C40), and 143 mM β-mercaptoethanol (βME, Sigma-Aldrich, cat#
674 444203) (Thevathasan et al., 2019). Stocks of enzyme solutions were prepared and stored at -
675 20°C as described in (Jimenez et al., 2020). GLOX/BME buffer was used for STORM imaging
676 of cells plated on coverslips.
677
678 GLOX/MEA STORM buffer was used for STORM imaging of cells plated in Ibidi glass bottom
679 8-well chambers (catalog # 80827). This buffer was prepared as above, but instead of βME, it
680 contained 50 mM mercaptoethylamine (MEA, Sigma-Aldrich, catalog # 30070) (Jimenez et al.,
681 2020). For double-color STORM imaging, we used the SMART Kit buffer (Abbelight).
682
683 **Antibodies**
684 All primary antibodies were checked for specificity on cells that were genetically-null for the
685 antigen (e.g., **Sup. Fig. 12**) and tissues: Fn1-null tissue sections obtained from Fn1-null
686 embryos were used to assay the specificity of each of the anti-Fn1 antibodies; Tissues isolated
687 from GFP-null, Itga5-null, and mCherry-null embryos were used to authenticate the specificity
688 of anti-GFP, anti-Itga5, and anti-mCherry antibodies. For each of the antibodies, staining of
689 control tissues resulted in no more fluorescent signal than the background fluorescence
690 produced by the use of secondary antibodies only. Rabbit polyclonal antibody R457 was raised
691 against the 70 kDa N-terminal domain of Fn1 (Aguirre et al., 1994; Sechler et al., 2001) and
692 rabbit polyclonal R184 was raised against the first six type III repeats of Fn1 (Raitman et al.,

693 2018). The specificity of these antibodies was verified by ELISA and Western blotting reporter

694 in the references in Table M2.

695

696 **Table M2. Antibodies**

Primary Antibodies (1º Ab)	Specificity	Source/ reference
Abcam recombinant rabbit monoclonal	Epitope recognized by this antibody is located within 301 aa between amino acids 1350- 1651 of mouse Fn1, transcript variant 2, mRNA, RefSeq NM_001276408	Abcam, cat # 199056
297.1 rabbit polyclonal	Raised to rat plasma Fn1. Recognizes multiple epitopes, see **Sup. Fig. 4**	Richard Hynes lab (Rickelt and Hynes, 2018)
R457 rabbit polyclonal	70 kDa N-terminal domain	Jean Schwarzbauer's lab (Aguirre et al., 1994; Sechler et al., 2001)
R184 rabbit polyclonal	First six type III repeats of Fn1	Jean Schwarzbauer's lab (Raitman et al., 2018)
3E2 mouse monoclonal	EIIIA	Sigma, cat #SAB4200784-100UL
GFP, chicken polyclonal	GFP	Aves, cat# GFP-1010;
GFP, rabbit polyclonal	GFP	MBL International; cat #598
Itgα5, rat monoclonal	Integrin alpha 5	BD biosciences, cat # 553319
mCherry, rabbit polyclonal	Cherry; tdTomato is composed of two mCherry molecules in tandem (Shaner et al., 2005)	Abcam, cat # ab167453

697

Secondary Antibodies (2° Abs)	Source, catalog #, concentration	Dilution
AffiniPure F(ab')$_2$ Fragment Donkey Anti-Rabbit IgG (H+L)	Jackson Immunoresearch, cat # 711-606-152, 1.5 mg/ml	1:300
Donkey anti-Mouse IgG (H+L) Highly Cross-Adsorbed Secondary Antibody, Alexa Fluor 555	ThermoFisher Scientific, A-31570, 2 mg/ml	1:300
Cy™3 AffiniPure F(ab')$_2$ Fragment Donkey Anti-Rat IgG (H+L)	Jackson Immunoresearch, 712-166-150, 1.5mg/ml	1:300
Alexa Fluor® 488 AffiniPure F(ab')$_2$ Fragment Donkey Anti-Chicken IgY (IgG) (H+L)	Jackson Immunoresearch, 703-546-155, 1.5mg/ml	1:300
Alexa Fluor® 647 AffiniPure F(ab')$_2$ Fragment Donkey Anti-Chicken IgY (IgG) (H+L)	Jackson Immunoresearch, 703-606-155, 1.5mg/ml	1:300
CF680 Donkey anti-rabbit, highly cross-adsorbed	Biotium, cat # 20418-50ul), 2mg/ml	1:200

698

699

700 **Epitope mapping of rabbit 297.1 polyclonal antibody.** Epitopes recognized by the
701 polyclonal 297.1 antibody were mapped by generating custom overlapping peptide arrays
702 (PEPperPRINT GmbH, Heidelberg). Fn1 protein sequence including alternatively-spliced
703 exons was encoded by 15-amino acid peptides with a peptide-peptide overlap of 13 amino

704 acids. The resulting Fn1 peptide microarrays contained 1,239 different peptides printed in
705 duplicate (2,478 peptide spots), and were framed by additional HA-tag (YPYDVPDYAG, 106
706 spots) control peptides. HA-tag peptide was used to monitor array quality and served as a
707 positive control for clean antibody binding detected with anti-HA-tag antibody (mouse
708 monoclonal anti-HA DyLight800 used at 0.5 µg/ml concentration). Prior to staining, arrays were
709 incubated with blocking buffer (Rockland, cat # MB-070) for 30 min at RT. To measure
710 background antibody binding, arrays were first incubated with secondary goat anti-rabbit IgG
711 (Fc) DyLight680 at 0.2 µg/ml concentration diluted in PBS, pH 7.4, containing 0.05% Tween 20
712 and 10% blocking buffer, and imaged. To determine specific 297.1 antibody binding, arrays
713 were incubated for 16 hours with shaking at 4°C with two dilutions of 297.1 antibody (1:300
714 and 1:1000). Antibody dilutions were made in PBS, pH 7.4 containing 0.05% Tween 20 and
715 10% blocking buffer (Rockland, cat # MB-070). Arrays were then washed with PBS, pH 7.4
716 containing 0.05% Tween 20 and incubated with goat anti-rabbit IgG (Fc) DyLight680 (0.2
717 µg/ml) for 45 min at RT. Arrays were then washed and imaged using LI-COR Odyssey Imaging
718 System; scanning offset 0.65 mm, resolution 21 µm, scanning intensities of 7/7 (red = 700
719 nm/green = 800 nm). Quantification of spot intensities and peptide annotation were done with
720 PepSlide® Analyzer.
721
722 **Embryo Staining** E9.5 embryos were isolated either from matings of wild-type C57BL6/J mice
723 or from mating Fn1$^{mEGFP/mEGFP}$ mice with wild-type mice to obtain Fn1$^{mEGFP/+}$ embryos.
724 Embryos were fixed using cold 4% PFA overnight at 4°C, washed 3 x 5 min in 1xPBS, and
725 blocked overnight at 4°C in blocking buffer containing PBS, 0.1% Triton-X, and 10% donkey
726 serum. Embryos were stained either with Abcam monoclonal anti-Fn1 antibodies at 1:300
727 dilution in blocking buffer or with both Abcam monoclonal anti-Fn1 antibodies and anti-GFP
728 antibodies at 1:300 dilution. The staining procedure was executed exactly as described in
729 (Ramirez and Astrof, 2020).

730

731 **Analysis of Fn1 matrix assembly and Western Blotting using MEFs** Matrix Assembly was
732 performed according to the established protocols (Wierzbicka-Patynowski et al., 2004). MEFs
733 were plated in 6-well dishes (9 cm^2 growth area) at a density of 2×10^5 cells per well for 48 h,
734 in complete medium and incubated under sterile conditions at 37°C, 5% CO2. Cells were
735 washed twice with ice cold PBS (supplemented with Mg^{2+} and Ca^{2+}), scraped with a cell
736 scraper and lysed with either 500 μl RIPA lysis buffer pH 8.0 (50 mM Tris-Cl, 150 mM NaCl, 2
737 mM EDTA, 1% v/v NP-40, 0.5% w/v sodium deoxycholate, 0.1% w/v SDS, 1X protease
738 inhibitor cocktail (Cell Signaling Technology, cat # 5871), or DOC lysis buffer, pH 8.8 (20 mM
739 Tris-Cl, 2 mM EDTA, 2% w/v sodium deoxycholate, 1X protease inhibitor cocktail (Cell
740 Signaling Technology, 5871). Extracts were carefully transferred to Eppendorf tubes containing
741 1 μl (250 units) Benzonase® Nuclease (Sigma-Aldrich, E1014), mixed by inverting a few times
742 and incubated at 37 °C for 15 mins. The samples were then centrifuged at 16,000 × g for 15
743 min at 4 °C. For cells lysed with DOC lysis buffer, the supernatant containing DOC-soluble
744 material was carefully removed, and the pellet containing the DOC-insoluble material was
745 resuspended in 100 μl SDS solubilization buffer, pH8.8 (20 mM Tris-Cl, 2 mM EDTA, 1% w/v
746 SDS, 1X protease inhibitor cocktail (Cell Signaling Technology, 5871). The DOC-insoluble
747 pellet was thoroughly dissolved by heating the sample to 95 °C and vortexing. All samples
748 were aliquoted and stored at -80 °C until further use. Prior to quantification of Fn1 in the
749 samples, the total protein concentration of the RIPA and DOC lysates was determined using
750 the BCA protein assay (Pierce™ BCA Protein Assay Kit, 23225). Lysates containing Fn1 and
751 Fn1-FP fusion proteins were reduced an resolved using 66-440 kDa Wes separation module
752 (ProteinSimple, SM-W007). Primary antibodies were used at the following dilutions: anti-total
753 Fn1 – 1:1000 (Abcam, ab199056), anti-GFP – 1:1000 (Roche, 11814460001), anti-mCherry –
754 1:1000 (Abcam, 167453). Primary antibodies were detected using horseradish peroxidase-

755 conjugated secondary antibodies (anti-Rabbit Detection Module ProteinSimple, DM-001), and
756 chemiluminescence was quantified using the Compass for SW software (v3.1.8). Prior to
757 running experimental samples, care was taken to optimize the dilutions of lysates to be within
758 the linear range of the detection.
759
760 **Analysis of Fn1 matrix assembly and Western Blotting using E9.5 embryos.** To analyze
761 Fn1-mEGFP matrix assembly *in vivo*, we mated $Fn1^{mEGFP/+}$ mice to obtain wild-type, Fn1
762 $^{mEGFP/+}$ and $Fn1^{mEGFP/mEGFP}$ littermate embryos. At the time of dissection, each embryo was
763 frozen on dry ice in individual Eppendorf tubes and stored at -80°C until the genotyping was
764 complete. Yolk sacs were used for genotyping. 300 μl of DOC ice-cold lysis buffer pH 8.8
765 containing protease inhibitors (see recipe above) were added to each embryo, and the
766 embryos were dissociated by passing through a 27-gauge syringe needle 5 times, keeping the
767 tubes on ice. Lysates were centrifuged at 16,000 × g for 15 min at 4°C. The supernatant
768 containing DOC-soluble material was transferred to another tube and was supplemented with
769 100 μl of 4x SDS loading buffer and β-mercaptoethanol (βME), at a final concentration of 350
770 mM of βME. The DOC-insoluble pellet was washed twice with 300 μl of DOC lysis buffer on
771 ice, and the pellet was then resuspended with 200 μl SDS solubilization buffer with protease
772 inhibitors (see recipe above). The pellet was dissolved by heating at 95°C and vortexing. And
773 supplemented with 66.6 μl of 4x SDS loading buffer and β-mercaptoethanol (βME), at a final
774 concentration of 350 mM of βME. Doc soluble and insoluble samples were heated at 95°C for
775 5 min and 40 μl were loaded on 4-12% acrylamide gel (Invitrogen cat # XP04120BOX). Fn1
776 was detected using rabbit anti-Fn1 1° antibody (Abcam, cat # 199056) and IRDye 680RD
777 Donkey anti-Rabbit 2° antibody (Licor, cat # #926-68073).
778 Membranes were imaged using Li-Cor Odyssey 9120 Gel Imaging System (#ODY-2425) and
779 quantified using Fiji software.

780

781 **Testing the reactivity of 297.1 polyclonal antibody to bovine Fn1 present in the fetal**
782 **bovine serum**. To test whether 297.1 antibody can bind bovine Fn1, we used a complete
783 medium (CM, see Table M1) and, as a control, a conditioned completed medium (CCM) which
784 we prepared by incubating 2×10^5 cells plated in a well of a 6 well plate for 48 hrs with 2 mL of
785 CM. CCM was centrifuged at 1000 rpm for 3 minutes to discard dead cells. 100 μL of
786 trichloroacetic acid (TCA) were added to 900 μL of CM or CCM to precipitate the protein and
787 incubated in ice for 30 min. Samples were centrifuged at 14000 rpm at 4C for 15 min. Pellets
788 were washed with 700 μL of 100% acetone and then resuspended in a gel loading buffer
789 containing 100 μl of 0.1N NaOH, 75 μl of 4X SDS-PAGE loading buffer, 0.35 M βME and
790 125 μl of H20. Samples were heated at 95°C for 5 min and 10 μl of each sample were resolved
791 using Novex™ WedgeWell™ 4 to 12%, Tris-Glycine, 1.0 mm, Mini Protein Gel (Invitrogen cat
792 # XP04120BOX) and run using Tris-Gly SDS Running buffer (Invitrogen, cat # LC2675).
793 Following the transfer to nitrocellulose membrane (Bio-Rad, cat # 1620122), Fn1 was detected
794 by immunoblotting using 1:1000 dilution of 297.1 polyclonal antibodies and IRDye 680RD
795 Donkey anti-Rabbit secondary antibody (Licor, cat # #926-68073). Protein standards were
796 from Invitrogen, cat # LC5925. Membranes were imaged using Li-Cor Odyssey 9120 Gel
797 Imaging System (#ODY-2425)

798

799 **Coating of coverslips with different ECM proteins** #1.5 round glass coverslips (Electron
800 Microscopy Sciences. Catalog # 72230-01) were coated with the following ECM proteins when
801 noted: gelatin (Sigma Aldrich, catalog # G2500) (0.1% (w/v) of gelatin was prepared in Milli-Q
802 water and autoclaved to dissolve), vitronectin (Sigma Aldrich, catalog # SRP3186; stock
803 solution was prepared as 200μg/ml in 0.1% BSA and water) and laminin (R&D systems,
804 catalog # 3400-010-02, stock 1 mg/ml was pipetted into 10ul aliquots and stored at -80°C). To

805 coat with gelatin, glass surfaces were incubated with the 0.1% gelatin solution for 5 min at
806 room temperature (RT). To coat with vitronectin or laminin, glass surfaces were incubated at
807 37° C for 1 hr in 20 μg/ml of either vitronectin or laminin, excess liquid was removed, cover
808 slips were rinsed once with 1X PBS, and blocked with 10 μg/ml heat denatured BSA for 30 min
809 before plating cells (Lu et al., 2020).

810 **MEFs plated on different substrata** MEFs were grown either on #1.5 round glass coverslips
811 in 24-well dishes or in 8-well glass Ibidi dishes depending on the experiment for the times
812 indicated in figure legends. MEFs were then rinsed with 1X PBS (warmed to 37^{0} C) for 5 min,
813 fixed with freshly thawed 4% PFA pre-warmed to 37^{0} C for 20 min, and washed three times
814 with 1X PBS (warmed to 37^{0} C) with mild shaking. All subsequent washing steps were done
815 with shaking. For permeabilization, cells were washed once in 1X PBS containing 0.1% Triton-
816 X 100 (PBST). Blocking was done for 30 min in 10% Donkey serum prepared in PBST
817 (blocking solution). After blocking, cells were incubated in primary antibodies diluted in
818 blocking solution overnight at 4^{0} C, as specified in **Table M2**. This was followed by 3 washes in
819 PBST for 10 min each. Cells were then incubated with secondary antibodies diluted in PBST
820 for 60 min at RT. Finally, cells were washed three times with PBST for 10 min each. DAPI
821 (1:300) was added to the second wash. Cells were mounted using Vectashield.
822

823 **Hydrogels**

824 **Methacrylated Alginate Synthesis:** Methacrylated alginate (MeAlg) was synthesized
825 according to a previously established protocol (Khetan et al., 2013). In brief, alginic acid sodium
826 salt from brown algae (Sigma-Aldrich, USA) (3% w/v) was fully dissolved in Dulbecco's
827 phosphate buffered saline (dPBS, Sigma-Aldrich, USA). Then, methacrylic anhydride (Sigma-
828 Aldrich, USA) (8% v/v) was added drop-wise to the alginate solution and stirred for 12 h at 4°C,
829 using 2M NaOH (Sigma-Aldrich, USA) to ensure that the pH remained between 8 and 9 for the

830 duration of the reaction. The resulting solution was passed through filter paper (GE Whatman)
831 and poured into Spectra/Por dialysis membrane with a 6–8 kDa molecular weight cutoff (Fischer
832 Scientific) and kept in DIW under stirring for 7 days to eliminate the unreacted MA and salts.
833 Dialyzed solution was then freeze-dried for 4 days to obtain MeAlg foam.

834 **Fabrication of the Hydrogel Substrates:** MeAlg substrates were fabricated using a previously
835 established protocol (Guvendiren and Burdick, 2012). Briefly, petri dishes with glass bottoms
836 were treated with UV/ozone (UVO) for 30 minutes, immediately followed by a coating of 3-
837 (trimethoxysilyl)propyl methacrylate (TMS) (Sigma-Aldrich, USA) to methacrylate the glass
838 surfaces (Guvendiren et al., 2009). The dishes were left in a desiccator overnight. The hydrogels
839 were fabricated using Michael-type addition polymerization. First, 2-hydroxy-4'-(2-
840 hydroxyethoxy)-2-methylpropiophenone (I2959) (Sigma-Aldrich, USA), a photoinitiatior (0.5%
841 w/v) was completely dissolved in Dulbecco's PBS (dPBS), followed by the lyophilized MeAlg (3%
842 w/v) synthesized previously. This was kept at room temperature until a clear solution was
843 achieved. Crosslinking occurs with the introduction of DL-Dithiothreitol (DTT) (Sigma-Aldrich,
844 USA) to the solution, along with 0.2M triethanolamine (Sigma-Aldrich, USA) at pH 10. To form
845 3kPa and 12 kPa gels, 20% and 30% (w/v) DTT are used, respectively. To promote cell
846 adhesion, GRGDSPC peptide (1% w/v) (Genscript) was added to the solution. After all contents
847 were thoroughly mixed, 5μL of MeAlg solution was pipetted onto the surface of the dish before
848 being covered with a glass coverslip in order to create gels less than 30μm thick. These were
849 left at room temperature for an hour to crosslink before being submerged in dPBS to remove the
850 coverslip.

851 **Atomic Force Microscopy** For stiffness measurements, hydrogel samples were submerged in
852 PBS and placed in a Dimension Icon AFM with ScanAsyst (Bruker). Using the PeakForce-QNM
853 mode, hydrogel samples were indented using an MLCT-Bio probe tip with pyramidal geometry
854 (Bruker, CA) and a nominal spring constant of 0.03 N/m, checked by thermal calibration.

855

856 **Treatment of cells with Deoxycholate (DOC)** 10^4 Fn1$^{mEGFP/+}$ MEFs were plated for 48 hrs in
857 8-well glass bottom Ibidi dishes in complete medium and incubated at 37° C and 5% CO_2. Two
858 hours before imaging SiR-actin was added at 1 μM final concentration. SiR-actin contains a
859 far-red dye, silicon rhodamine, conjugated to jasplakinolide that labels F-actin in live and fixed
860 cells (Lukinavicius et al., 2014). Just before imaging, complete medium was replaced by 150 μl
861 imaging medium containing 33 μg/ml of Hoechst 33342. Positions were marked in each well
862 and live imaging was initiated at 37°C and 5 % CO_2 humidified chamber. After 15 min, 150 μl
863 4% DOC solution prepared in imaging medium containing 33 μg/ml Hoechst was added to the
864 experimental well (final pH 8.01) and 150 μl imaging medium containing 33 μg/ml Hoechst but
865 without DOC was added to the control well. Cells were imaged at 50 sec intervals until F-actin
866 and DNA disappeared (see Movie 4). The medium was then removed, cells were rinsed for 1
867 min with 1X PBS pre-warmed to 37°C, fixed with 4% PFA pre-warmed to 37°C. For staining,
868 cells were permeabilized and blocked as above, and then incubated with Abcam monoclonal
869 anti-Fn1 antibody diluted 1:300 dilution in the blocking solution at 4°C overnight. Primary
870 antibodies were detected with anti-rabbit secondary antibodies conjugated to AlexaFluor647.
871 Enhanced-resolution imaging was used to image the DOC-treated fibrils, as described below.

872 **Confocal settings for enhanced resolution imaging** Confocal images of fixed samples were
873 recorded using Nikon A1-HD25 inverted confocal microscope equipped with CFI
874 Apochromat TIRF 100xC Oil objective with the pinhole set to 0.8 Airy units, and imaged
875 through 2 – 4 microns with step size of 0.125 μm - 0.15 μm at a sampling of 40 nm per pixel
876 and 180 nm optical resolution. Deconvolution was done using Nikon 3D deconvolution
877 software (v5.11.01). Airyscan imaging was performed using Zeiss LSM 880 fitted with a 32

878 array AiryScan GaAsP-PMT detector and the Plan Apochromat 63X Oil (NA 1.4) objective.
879 Deconvolution and pixel reassignment were done using Zeiss LSM software.
880
881 **Quantification of effective labeling efficiency and the number of Fn1 molecules in Fn1**
882 **nanodomains.** To quantify the number of Fn1 molecules per nanodomain and to measure
883 effective labeling efficiency, we used Nup96-mEGFP U2OS cells as a reference cell line and
884 SMAP software (Ries, 2020; Thevathasan et al., 2019). In Nup96-mEGFP cells, two copies of
885 the nucleoporin Nup96 gene are tagged with the monomeric enhanced green fluorescent
886 protein (mEGFP) at the C-terminus of the Nup96 gene, generating Nup96-mEGFP fusion
887 protein (Thevathasan et al., 2019). The stoichiometry of Nup96-mEGFP in nucleopores is well
888 characterized, and careful measurements, imaging methodology, and software have been
889 developed (Diekmann et al., 2020; Ries, 2020; Thevathasan et al., 2019). Together, these
890 tools allow the use of Nup96-mEGFP cell line as a reference to assess the quality of SMLM
891 imaging protocol, measure effective labeling efficiency, and determine the number of Fn1-
892 mEGFP molecules in Fn1 nanodomains.
893
894 Nup96-mEGFP cells (clone #195, Cell Line Services, CLS, clsgmbh.de, catalogue no. 300174)
895 were cultured according to the vendor's specifications in McCoy's 5a medium. Fn1-mEGFP
896 MEFs were cultured in complete DMEM as described above. $3x10^5$ Nup96-mEGFP cells and
897 $5x10^4$ Fn1-mEGFP cells were plated in their specified culture medium on 25 mm high precision
898 glass cover slips #1.5H (Marienfeld ref# 0117650, obtained from Azer Scientific, PA, USA, cat
899 # ES0117650) positioned in 6-well plates (Corning, cat # 353046). Prior to their use, glass
900 cover slips were cleaned using concentrated nitric acid, washed in water, and autoclaved, as
901 described in (Kaech and Banker, 2006). Coverslips were used without coating. 24 hours after
902 plating, cells were fixed and stained as described in (Thevathasan et al., 2019) with minor
903 modifications. Cover slips with Nup96-mEGFP cells and Fn1-mEGFP cells were handled

904 contemporaneously in pairs at each step. For fixation, permeabilization and washing,
905 coverslips were kept in 6-well plates. Cells were fixed in PBS containing 2.4% PFA for 20 min
906 at RT. PFA was aspirated and cells were incubated with 100mM NH_4Cl in PBS for 5 min at RT,
907 and then washed 3 x 5 min in PBS with agitation. Cells were permeabilized for 20 min at RT
908 using PBS containing either 0.2% Triton-X for Nup96-mEGFP cells or 0.1% Triton-X for Fn1-
909 mEGFP. Cells were then washed in PBS 3 x 5 min at RT, and washed once more for 5 min in
910 PBS containing 0.1% Triton-X, and then either used immediately for staining, or stored at 4°C
911 in PBS containing 0.1% Triton-X (PBST) until further use. For each experiment, sufficient
912 amounts of each solution were prepared such that Nup96- mEGFP and Fn1-mEGFP cells
913 were incubated with the same mixtures. Solutions containing blocking reagents and antibodies
914 were spun for 5 min at top speed using tabletop centrifuges to get rid of particulates.
915 Humidified chambers were prepared from empty pipet tip boxes with water placed in the lower
916 chamber and parafilm partially covering the surface of the tip rack. Drops of solutions were
917 placed on the parafilm, and cells were incubated with various solutions by inverting coverslips
918 on top of the droplets. To block non-specific antibody binding, cells were first incubated with a
919 blocking solution (10% donkey serum in PBST) for 30 min at RT. Cover slips were then gently
920 lifted, drained, and incubated with anti-GFP antibody (Aves lab, cat# GFP-1010) diluted 1:100
921 in the blocking solution overnight at 4°C. Coverslips were then placed into 6-well plates and
922 washed 3 x 5 min in PBST with agitation. Cells were then incubated with Alexa-647-conjugated
923 anti-chicken $F(ab)_2$ (Jackson ImmunoResearch 703-606-155) diluted 1:300 in the blocking
924 solution for 4 hours at RT, and then washed 3 x 5 min in PBST with agitation. Stained
925 coverslips were stored at 4°C until imaging.
926
927 **Preparation of cover slips for SMLM imaging** Coverslips with plated cells were rinsed with
928 GLOX/BME buffer and mounted onto single cavity glass slides (VWR, cat #10118-600), pre-
929 filled with 80 μl GLOX/BME buffer immediately prior to the placement of coverslip. Excess

930 buffer was fully adsorbed from the sides and the top of the coverslip with Whatman paper,
931 taking care to keep the coverslip centered on top of the cavity. Coverslips were sealed onto the
932 cavity slide by pipetting Acid-Free Elmer's No-Wrinkle Rubber Cement (Amazon.com,
933 https://www.amazon.com/Elmers-No-Wrinkle-Rubber-Cement-Acid-
934 Free/dp/B014JUDMBA/ref=sr_1_2?keywords=Elmer%27s+No-
935 Wrinkle+Rubber+Cement%2C+Acid-Free&qid=1637633240&sr=8-2) around the edge, and
936 allowing the rubber cement to cure for ~15 min. After imaging, rubber cement was gently
937 peeled off, and the slides were soaked in PBST for 5 min at RT to remove cover slips which
938 were then stored in 6-well plates filed with PBST containing 0.02% NaN_3 at 4°C until further
939 use. In this set up, the GLOX/BME buffer remained at pH 8 for at least 12 hours.
940
941 **SMLM imaging protocol I: Quantification of the effective labeling efficiency and the**
942 **number of mEGFP molecules in Fn1-mEGFP nanodomains.** For the following experiments,
943 2D imaging was used to maximize the resolution in the plane of imaging. To minimize
944 fluorophore bleaching and maximize the number of collected photons we followed the protocol
945 protocol developed by (Diekmann et al., 2020). Stained Nup96-mEGFP and Fn1-mEGFP cells
946 were imaged in pairs using the same preparation of the GLOX/BME buffer and the same
947 imaging conditions (described below). For each independent experiment (n=4) and for each
948 round of measurements, images of Nup96-mEGFP and Fn1-mEGFP cells taken on the same
949 day were analyzed. SMLM was performed using Nikon A1-HD25 Ti2E microscope equipped
950 with motorized TIRF illumination, 125mW 640 nm solid-state laser, Perfect Focus, and CFI
951 Apochromat TIRF 100xC Oil objective with numerical aperture 1.49 (cat # MRD01905). All
952 images were acquired at the critical angle of incidence (57°) and recorded using a 512 x 512
953 EMCCD camera (Princeton Instruments), using 128 x 128 central region on the camera. Gain
954 was set to 3, multiplication gain amplifier was set to 20 MHz. Prior to acquisition, the centered
955 ROI (128 x 128) was bleached at 57° angle, and 10% laser power for 500 frames followed by

956 additional 500 frames at 20% laser power, with the exposure of 60 ms per frame. Images were
957 then acquired at 57° angle, 20% laser power, for 60,000 frames at 60 ms per frame. Images
958 were processed, rendered, and quantified using SMAP and Matlab version 2020a (Ries,
959 2020), as described (Diekmann et al., 2020) and the documentation found on
960 https://github.com/jries/SMAP. Settings for peak finding in the SMAP software were set
961 according to our camera's manufacture's specifications and were the following: EM was set to
962 "on", camera pixel size was set to 0.162 μm, EM gain was set to 300, e-/ADU conversion factor
963 was set to 2.35. Data was fitted using a Gaussian PSF model, the cutoff parameter for peak
964 finding was set to 2, and ROI size was set to 7 pixels. Localizations were then grouped and
965 rendered, using default parameters in SMAP. Drift correction was performed on rendered
966 localizations in timepoint blocks of 10 or 20, as recommended (Thevathasan et al., 2019) and
967 https://github.com/jries/SMAP. Following satisfactory drift correction judged by the overlapping
968 cross-correlations, localizations were filtered according to the recommended settings for Alexa-
969 647 fluorophore (Thevathasan et al., 2019); In brief, localizations with poor precision were
970 filtered out by limiting localization precision to 0 – 15 nm, out-of-focus localizations were
971 excluded by setting the PSF range to 0 – 150 nm in the x-y plane, poorly fitted localizations
972 were further filtered out by setting the LLrel parameter (relative log-likelihood) in SMAP to a
973 negative cut-off value leaving the majority of the peak intact, and the first 1000 frames were
974 excluded from the analyses. All the remaining grouped localization were rendered according to
975 $\sqrt{photons}$ and images were color-coded using LUTs set according to localization density.
976
977 Image resolution was measured using the Fourier Ring Correlation (FRC) method described
978 by (Nieuwenhuizen et al., 2013) and implemented in SMAP. Voronoi cluster discovery was
979 performed according to (Andronov et al., 2016a) and their algorithm implemented in SMAP.
980 DBSCAN cluster analysis was performed according to (Caetano et al., 2015; Ester et al., 1996)

981 implemented in SMAP; For DBSCAN, the minimum number of points in the neighborhood (k)
982 was set to 4, as recommended for all 2-dimentional data (Ester et al., 1996). The
983 neighborhood radius ε was set either to 14 nm (the average apparent radius of Fn1
984 nanodomains determined as described below) or automatically estimated by the DBSCAN
985 algorithm in SMAP (Ries, 2020).
986
987 NPC radius, effective labeling efficiency and the number of gourped localizations per
988 fluorophore were determined using the algorithm in SMAP following the published automated
989 workflow to segment and analyze nucleopore complexes (NPCs), using the parameters
990 recommended by (Thevathasan et al., 2019) without modifications. In brief, NPCs in focus
991 (mean fitted PFS size of each NPC was less then 145 nm) were automatically segmented
992 using circular ROI of 220 nm in diameter. The number of grouped localizations per NPC, NPC
993 radius, and effective labeling efficiency (ELE) were determined using published algorithms
994 implemented in SMAP without modifications, as described in (Diekmann et al., 2020;
995 Thevathasan et al., 2019) and the SMAP user manual “Analysis of NPCs using SMAP”. Since
996 we used identical staining, imaging, and processing parameters for Nup96-mEGFP and Fn1-
997 mEGFP cells, the number of Fn1-mEGFP molecules per nanodomain was calibrated to the
998 number of grouped localizations per NUP96-mEGFP protein, as described (Thevathasan et al.,
999 2019). In brief, we first determined the number of merged localizations per NPC in the ROI
1000 (L_{ref}). Each NPC contains 32 NUP96-mEGFP proteins, therefore, the number of merged
1001 localizations per Nup96-mEGFP (N_{ref}) is $N_{ref}= L_{ref}/32$. To determine the number of Fn1-mEGFP
1002 proteins per Fn1 nanodomain, we segmented Fn1 nanodomains manually using a circular ROI
1003 of 60 nm in diameter and the number of merged localizations per ROI (L_t) was determined by
1004 using the *countingStatistics plugin* in SMAP, as outlined in the SMAP manual “Analysis of

1005 NPCs using SMAP". The number of Fn1-mEGFP proteins per nanodomains (N_t) is L_t / N_{ref}.
1006 Since Fn1 is only secreted as a dimer, the number of Fn1 dimers per nanodomain is N_t /2.
1007
1008 Nanodomain periodicity in Fn1 fibrils stained by a variety of different antibodies was assayed
1009 and quantified according to (Fruh et al., 2015). In brief, MEFs were stained using a variety of
1010 antibodies at different dilutions, or using combinations of antibodies, as noted in **Figs. 5, 6, 8**,
1011 according to the staining protocol described above and imaged using GLOX/BME buffer and
1012 the exact imaging settings as described for imaging Nup96-mEGFP and Fn1-mEGFP cells
1013 stained with anti-GFP antibodies (see above). Images were processed and rendered in SMAP
1014 according to the parameters described above. Gaussian rendering of the localizations (min σ
1015 Gaussian was set to 3nm) were saved as uncompressed tiff files and opened in Fiji version
1016 2.1.0/1.53c, intensity line profiles along each fibril were generated and imported into Matlab
1017 2021a. To assay periodicity, we used the autocorrelation function implemented in the Matlab's
1018 2021a Econometrics toolbox and the criteria outlined in (Fruh et al., 2015). In brief, the
1019 presence of at least four regularly-spaced peaks in the autocorrelation profile was considered
1020 to reflect the periodical nature of Fn1 nanodomains, and the position of the first autocorrelation
1021 maximum was taken as a quantitative measure of nanodomain periodicity, as extensively
1022 discussed and computationally modelled in the Supplemental Data section of (Fruh et al.,
1023 2015). Ljung-Box Q-test for residual autocorrelation was performed using Matlab's 2021a
1024 Econometrics toolbox to assess statistical significance of autocorrelation.
1025 To determine the apparent diameter of Fn1 nanodomains, we imported fibril intensity
1026 line profiles obtained from SMLM images of $Fn1^{mEGFP/mEGFP}$ MEFs stained for GFP into Matlab
1027 2021a. To automate the analyses, we used Signal Processing toolbox in Matlab 2021a to fit
1028 each intensity peak in the line profile with a Gaussian curve and calculate full width at half
1029 height (FWHT) for each peak. Altogether, 1292 nanodomains in 27 long (> 1 μm in length)

1030 fibrils from six cells and 3 independent experiments were assessed. We have also performed
1031 this analysis manually on a subset of Fn1 nanodomains (n=248) in long fibrils by fitting a
1032 Gaussian to an intensity profile of each individual nanodomain and calculating FWHT. The
1033 results were the same.
1034
1035 **Assembly of exogenously-added Fn1: Part I, Live Imaging** 3-well culture insert (Ibidi, cat #
1036 80366) was placed in the middle of the 35 mm glass-bottom dish (Ibidi, cat # 81158) and then
1037 0.8 x 10^6 Fn1-tdTomato-expressing MEFs were plated surrounding the inserts and cultured for
1038 24 hours to reach confluency and establish Fn1-tdTomato matrix. At a 24-hour time point, Fn1-
1039 mEGFP-expressing MEFs were plated inside the inserts on glass without coating for 5 hours.
1040 Prior to imaging, the culture medium was removed and replaced with the imaging medium.
1041 Live imaging was performed using Plan Fluor 40x Oil (numerical aperture 1.3). Positions
1042 containing Fn1-mEGFP-expressing MEFs were imaged at ~17-18 min intervals for ~16 hours
1043 in humidified Tokai Hit stage-top incubator at 5% CO_2. Each position was imaged 40-43
1044 confocal slices at 0.5 μm thickness, the pinhole was set to 1 Airy unit.
1045
1046 **Assembly of exogenously-added Fn1: Part II, SMLM** The medium containing secreted Fn1-
1047 tdTomato fusion proteins was collected after a 72-hour culture of confluent Fn1-tdTomato
1048 MEFs generated by CRISPR/Cas9 mutagenesis, as described above. The medium was spun
1049 at 300 x *g* for 5 min to pellet debris. The concentration of Fn1-tdTomato in the supernatant was
1050 quantified using ELISA kit using antibodies specific to mouse Fn1, which does not cross react
1051 with bovine Fn1 (Abcam, cat # ab21097). Fn1-tdTomato-containing supernatant was diluted 4-
1052 fold with fresh MEF culture medium to the final concentration of 5 μg/ml of Fn1-tdTomato, and
1053 2 ml of this supernatant were added to Fn1-mEGFP MEFs plated on 25 mm 1.5H glass
1054 coverslips the day before at 10^5 cells per well in a 6-well plate. Following 24-hours of

1055 incubation at 37°C and 5% CO_2, cells were washed with PBS and fixed in 4% PFA in PBS for
1056 20 min at RT. PFA was quenched with 100mM NH_4Cl in PBS, cell were washed 3x5 min in
1057 PBS, and permeabilized with PBS containing 0.1% Triton-X (PBST). Cells were then incubated
1058 with a blocking solution containing 10% donkey serum in PBST for 30 min at RT. To detect
1059 Fn1-tdTomato, cells were incubated at 4°C overnight with rabbit anti-mCherry antibody
1060 (Abcam, cat #ab167453) diluted 1:100 in the blocking solution. Primary antibodies were
1061 detected with Alexa-647-conjugated donkey anti-rabbit $F(ab)_2$ secondary antibodies (Jackson
1062 laboratories, cat # 711-606-152) diluted 1:300 in blocking solution and incubated for 4 hrs at
1063 RT. Cells were then washed 3x5min in PBST and stored at 4°C until imaging. dSTORM
1064 imaging was performed using GLOX/BME buffer. Cell were imaged at 57° angle using the
1065 SMLM imaging protocol, as described above. Images were processed and reconstructed using
1066 SMAP using the same parameters, as described above.
1067
1068 **Live imaging using TIRF** $Fn1^{mEGFP/+}$ MEFs were plated on 35-mm round glass bottom Mattek
1069 dishes (catalog # P35G-1.5-14-C), complete medium was switched to imaging medium prior to
1070 filming. Live TIRF microscopy was performed using Nikon A1-HD25 inverted confocal
1071 microscope equipped with 4 laser lines of 100mW per line at 405, 488, and 561nm and
1072 125mW at 640nm, and motorized TIRF illumination. CFI Apochromat TIRF 100xC Oil objective
1073 and EMCCD camera were used. Before imaging lasers were aligned and the critical angle of
1074 incidence for imaging was determined by the software. The exposure time was 20 ms and
1075 readout speed was set at 10 MHz.
1076
1077 **Live imaging using confocal point-scanning microscopy** Live cell imaging was performed
1078 using Ibidi glass bottom 8-well chambers (catalog # 80827). $0.6*10^4$ wild-type or $Fn1^{mEGFP/+}$
1079 MEFs were plated on glass in each well of Ibidi glass bottom 8-well chambers and allowed to
1080 grow overnight prior to staining and imaging by direct Stochastic Optical Reconstruction

1081 Microscopy (dSTORM), see SMLM imaging protocol II below. For FUD and III-11C treatment,
1082 Fn1$^{mEGFP/+}$ MEFs were plated in 8-well glass Ibidi dishes (1 cm^2 growth area) without coating at
1083 a density of $0.6x10^4$ cells/well in complete medium. After 5 hours, DMEM was removed and
1084 cells were rinsed once with 1X PBS. Subsequently, the medium was changed to imaging
1085 medium. For FUD experiments, imaging medium was supplemented either with 225 nM FUD
1086 or 274 nM of control III-11C peptide. Untreated wells contained cells incubated with imaging
1087 medium. Following the addition of the imaging medium (with or without the peptides), the
1088 chamber was immediately set up for imaging in the humidified Tokai Hit stage-top incubator at
1089 37°C, 5% CO_2. Live imaging was performed using Nikon A1-HD25 inverted confocal
1090 microscope with the DUG 4-Channel Detector and 2 GaAsP, 2 high-sensitivity PMTs, and a
1091 motorized XYZ stage with Nikon's Perfect Focus 4 system, and Plan Fluor 40x Oil (numerical
1092 aperture 1.3, cat # MRH01401). mEGFP was excited using 488 nm laser at 1% power and
1093 pinhole set to 1 Airy unit. An optical zoom of 2 and Z step size of 0.5 μm were used, and stack
1094 size was set to 10-15 microns allowing to image the entire cell. For overnight movies, each
1095 position was filmed every 1.5 min – 4 min, as noted in Movie legends. Movies in the mp4
1096 format were generated using Imaris 9.5.1 (Bitplane), titles and arrows were added using Adobe
1097 Premiere Elements Editor 2020.
1098
1099 **SMLM imaging protocol II: Imaging cells plated on Ibidi glass-bottom dishes.** This
1100 protocol was used to image cells following the live DOC assay or overnight live imaging (**Fig.**
1101 **10** and **Sup. Fig. 9**). Following fixation with 4% PFA, cells were washed with PBS, incubated
1102 with blocking buffer containing PBS, 0.1% Triton-X, and 10% donkey serum for 30 min at RT.
1103 Cells were then incubated with Abcam monoclonal anti-Fn1 antibody diluted at 1:300 in
1104 blocking buffer overnight at 4°C. Following three washes at 5 min each in PBST (PBS with
1105 0.1% TritonX), cells were incubated with Alexa-647-conjugated anti-rabbit secondary

1106 antibodies diluted 1:300 in blocking buffer for 4 hours at RT, and washed three washes at 5
1107 min each in PBST. Prior to imaging, freshly prepared GLOX/MEA buffer was added and the
1108 chamber was immediately sealed using parafilm. STORM was performed using Nikon A1-
1109 HD25 Ti2E microscope equipped with motorized TIRF illumination, 125mW 640 nm solid-state
1110 laser, Perfect Focus, and a 100x/1.49NA objective. Images were acquired at the critical angle
1111 of incidence and recorded using a 512 x 512 EMCCD camera (Princeton Instruments).
1112 Calibration was obtained by imaging of 100 nm Tetraspeck beads (Life technologies, catalog #
1113 T-7279) using the same glass surface and buffer conditions. To drive Alexa-647 into the dark
1114 state, samples were pre-bleached by the illumination at 640 nm for 10 seconds at 100 % laser
1115 power. 40,000 frames were acquired at 8.4 ms exposure. Blinking events were fitted using the
1116 Nikon N-STORM localization software. Images were analyzed using Nikon software (Nikon
1117 Elements AR Software v5.11.01). Localization events with fewer than 800 or more than 50000
1118 photons were filtered out to remove blinking evens that were either too faint or too bright
1119 (Jimenez et al., 2020). In addition, blinking events were filtered out if they occurred in more
1120 than 5 consecutive frames or where outside the z-range determined by the calibration using
1121 100 nm Tetraspeck beads. Images in which z-rejection was below 50% were used for further
1122 analyses.
1123
1124 **Analysis of localization numbers in fibrillar and non-fibrillar nanodomains** In order to
1125 enrich for non-fibrillar nanodomains, Fn1$^{mEGFP/+}$ MEFs were plated in 8 well glass Ibidi dishes
1126 (1 cm^2 growth area) without coating. Cell were plated at the density of $0.6x10^4$ cells/well in
1127 imaging medium with or without FUD (225 nM) or III-11C (274 nM), and incubated in at 37°C,
1128 5% CO_2 for 1 hr. Subsequently, MEFs were rinsed once in warm 1X PBS and fixed using pre-
1129 warmed 4% PFA for 20 min. After fixation, wells were rinsed three times, 5 min each with Stain
1130 Buffer (cat # 554656 BD Pharmingen), blocked for 30 min at room using 5% Donkey serum
1131 prepared in Stain Buffer, and incubated with the monoclonal anti-Fn1 (Abcam, cat # 199056)

1132 overnight at 4º C. Cell were then washed with Stain Buffer three times, 10 min each, and
1133 incubated with anti-rabbit antibodies conjugated with Alexa-647 for 1 hour at rt. Cell were then
1134 rinsed again with Stain Buffer three times, 10 min each, and stored at 4º C in 1X PBS. STORM
1135 imaging was performed, as described in SMLM imaging protocol II. To quantify the number of
1136 grouped localizations per nanodomain, we used the free-hand ROI tool in the STORM window
1137 (Nikon Elements AR Software v5.11.01) to determine the number of localizations within non-
1138 fibrillar and fibrillar Fn1 nanodomains. Fn1 nanodomains were analyzed in 5 random regions
1139 from 3 independently acquired images (a total of 15 fields) for each sample. To determine the
1140 number of localizations in Fn1 nanodomains within fibrils, we analyzed more than 20 from 3 or
1141 more independently acquired images. All the counts were plotted in Prism 8.2.1 (GraphPad
1142 Software, USA), and compared using either one-way ANOVA test with Tukey's correction or
1143 Kruskal-Wallis test with Dunn's correction for multiple testing.
1144
1145 **Double-color dSTORM acquisition** Samples were mounted with the SMART Kit buffer
1146 (Abbelight). 2D or 3D STORM images were acquired using a SAFe360 module (Abbelight)
1147 coupled to an inverted bright-field Olympus IX83 microscope, equipped with a 100X oil-
1148 immersion objective (1.49 NA). This dual-cam system (sCMOS cameras, Orcaflashv4,
1149 Hamamatsu) allows to perform multicolor STORM by spectral demixing strategy coupled to the
1150 use of far-red dyes (BioOptics World, 2021, Caorsi and Karlsson).
1151 Briefly, a dichroic at 700nm is used to separate the fluorescence emission from AF647 and
1152 CF680 dyes. The Point Spread Function (PSF) of each detection can be retrieved on both
1153 cameras and the measured photon numbers is related to the spectral separation of the
1154 fluorophore (**Fig. M1**).
1155

We acquired 60000 frames at 20ms exposure time on a camera sensor size of 1024x1024 pixel to collect single-molecule detections. The irradiation at the sample was tuned according ASTER technology (Mau et al., 2021) implemented on the SAFe360 Abbelight module. Resulting coordinate tables and images were processed and analyzed using NEO software (Abbelight).

As the PSF is captured on both cameras, transmitted and reflected, a ratiometric analysis is applied: a ratio for each detection is calculated and the final ratio distribution is used for lambda assignment:

$$R_{A,i} = \frac{I_{R,i}}{I_{R,i} + I_{T,i}}$$

where the suffix A is the fluorophore, i the localisation and I_R and I_T the intensity measured on

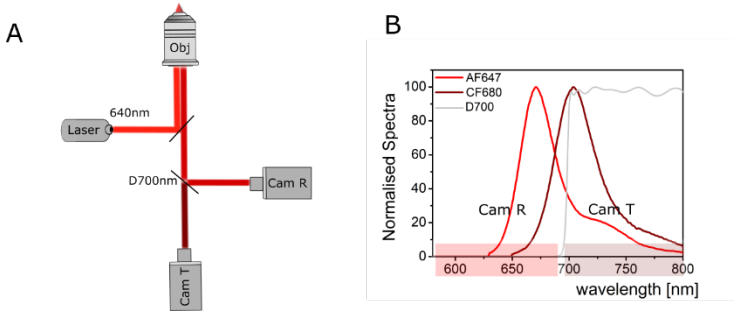

Figure M1. Spectral de-mixing optical scheme. A. A 640 nm laser is sent through the objective lens to excite AF647 and CF680 fluorophores. The emitted light is separated by a 700 nm long pass dichroic filter that reflects light below 700 nm into the Reflected camera (Cam R) and transmits light above 700 nm into the Transmitted camera (Cam T). **B.** Emission spectra of AF647 and CF680 dyes together with a 700nm dichroic filter showing spectral separation into the two cameras Cam R and Cam T.

camera R and camera T (i.e. the number of photons emitted per molecule).

1170 Average ratio distributions obtained from measurements are shown in **Fig.M2**:

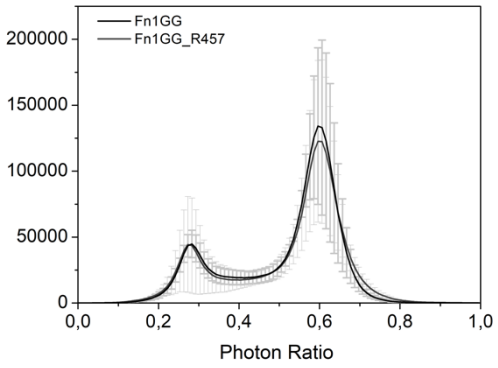

Figure M2. Average ratio distributions for Fn1$^{mEGFP/mEGFP}$ cells stained using chicken anti-GFP and rabbit anti-GFP antibodies (Fn1GG, dark gray) or chicken anti-GFP and rabbit R457 antibodies (Fn1GG_R457, lighter gray). The two fluorophore populations can be clearly distinguished for lambda assignment.

1171
1172
1173 Following the ratio distributions measured on the samples the following parameters have been
1174 used for separation: detections with ratios between 0-0.45 were assigned to CF680 and
1175 detections with ratios between 0.5-1 were assigned to AF647. On average 3% of detections
1176 were rejected while keeping crosstalk below 1%. Following de-mixing, colocalization analysis
1177 was performed using Neo software following the CBC algorithm (Malkusch et al., 2012).
1178 Parameters set for CBC analysis were R_{max} at 300 nm and the number of steps equal to 10. In
1179 addition the CBC algorithm as implemented in ThunderSTORM, with R_{max} = 50 nm, and the
1180 number of steps equal to 10 (Ovesny et al., 2014) was used to perform CBC analyses (Malkusch
1181 et al., 2012).

1182

1183 **Supplemental Material:** 12 Figures, 6 movies

1184

1185 **Figure Legends are included next to each figure**

1186

1187 **Legends for Movies**

1188 **Movie 1. Rotational views through the Fn1+ ECM in the cardiac jelly.** The whole E9.5
1189 embryo was stained using Abcam rabbit monoclonal anti-Fn1 antibody and imaged using 100x
1190 objective, N.A. 1.49, with the pinhole set at 0.8 Airy units, and sampling of 40 nm per pixel in x,
1191 y. The movie shows 3D reconstruction through 3.4 μm of tissue sampled every 0.121 μm in z.
1192 Fn1 is in white, DAPI is in blue. Arrows point to examples of beaded Fn1 fibrils.
1193
1194 **Movie 2. Fn1 fibrillogenesis imaged by TIRF microscopy.** $Fn1^{mEGFP}$ MEFs were transiently
1195 transfected with mCardinal-Lifeact, plated on gelatin-coated glass coverslips, and imaged 48
1196 hours later. Filming was done every 2 min for 30 min using TIRF and 100x objective, N.A.
1197 1.49. The first set shows the Fn1-mEGFP channel. Yellow arrows point to centripetally-moving
1198 Fn1 nanodomains organized into an elongating linear fibril. The second set is an overlay
1199 between Fn1-mEGFP and mCardinal-Lifeact.
1200
1201 **Movie 3. 2% DOC dissolved cytoplasm and nucleus in under 13 min leaving cell-free Fn1**
1202 **fibrils.** MEFs expressing Fn1-mNeonGreen were plated on glass-bottom slides without coating
1203 and labeled with SiRActin (magenta) to visualize F-actin, and Hoechst (blue) to visualize DNA.
1204 Time-lapse was recorded every 54 sec immediately following the addition of the DOC solution
1205 pH 8.01 to live cells. The presence of 2% DOC dissolves actin cytoskeleton and nuclei and
1206 leaves cell-free Fn1 ECM fibrils (green). Fn1 fibrils collapse following the dissolution of the
1207 actin cytoskeleton due to the loss of tension.
1208
1209 **Movie 4. Fibrillogenesis of ectopic Fn1.** 3-well culture insert was placed in the middle of the
1210 35 mm glass-bottom dish and 0.8 x 10^6 Fn1-tdTomato-expressing MEFs were plated
1211 surrounding the inserts. 24 hours later, Fn1-mEGFP-expressing MEFs were plated inside the
1212 inserts on glass without coating for 5 hours. Confocal live imaging of areas containing Fn1-

1213 mEGFP-expressing MEFs was performed using Plan Fluor 40x Oil (NA 1.3). Positions
1214 containing Fn1-mEGFP-expressing MEFs were imaged at 17-18 min intervals for ~16 hours.
1215 This movie contains maximum intensity projections composed of forty-three confocal slices at
1216 0.5 μm thickness, the pinhole was set to 1 Airy unit. The first still panel in this movie is a
1217 montage of the plate to show Fn1-tdTomato and Fn1-mEGFP-expressing cells prior to the start
1218 of the time-lapse.
1219
1220 **Movie 5. Cells incubated with 11-IIIC, show robust fibrillogenesis.** $Fn1^{mEGFP/+}$ MEFs were
1221 plated on uncoated glass in 8-well Ibidi chambers for 4 hours. Medium containing 11-IIIC
1222 control peptide was then added and cells were filmed every 90 sec for about 15 hours, as
1223 described in Methods. The movie begins approximately 30 min after the 11-IIIC-containing
1224 medium was added, the time it takes to set up time-lapse recording. Arrows point to the cell
1225 periphery and examples of centripetally moving Fn1 fibrils.
1226
1227 **Movie 6. FUD interferes with linking centripetally moving Fn1+ nanodomains into fibrils.**
1228 $Fn1^{mEGFP/+}$ MEFs were plated on glass in 8-well Ibidi chambers for 4 hours. Medium containing
1229 FUD peptide was then added and cells were filmed every 3 min for about 15 hours, as
1230 described in Methods. The movie begins approximately 30 min after the FUD-containing
1231 medium was added, the time it takes to set up time-lapse recording. Note the dismantling of
1232 pre-existing fibrils at the beginning of the movie. Yellow and red arrows point to the cell
1233 periphery. Note the presence of centripetally moving Fn1-mEGFP “beads” and the scarcity of
1234 Fn1 fibrils for the majority of the duration of the movie.
1235

1236 **References**

1237 Aguirre, K.M., R.J. McCormick, and J.E. Schwarzbauer. 1994. Fibronectin self-association is
1238 mediated by complementary sites within the amino-terminal one-third of the molecule. *J Biol*
1239 *Chem*. 269:27863-27868.

1240 Akimov, S.S., D. Krylov, L.F. Fleischman, and A.M. Belkin. 2000. Tissue transglutaminase is
1241 an integrin-binding adhesion coreceptor for fibronectin. *J Cell Biol*. 148:825-838.

1242 Andronov, L., Y. Lutz, J.L. Vonesch, and B.P. Klaholz. 2016a. SharpViSu: integrated analysis
1243 and segmentation of super-resolution microscopy data. *Bioinformatics*. 32:2239-2241.

1244 Andronov, L., I. Orlov, Y. Lutz, J.L. Vonesch, and B.P. Klaholz. 2016b. ClusterViSu, a method
1245 for clustering of protein complexes by Voronoi tessellation in super-resolution microscopy. *Sci*
1246 *Rep*. 6:24084.

1247 Arai, Y., R. Yasuda, K. Akashi, Y. Harada, H. Miyata, K. Kinosita, Jr., and H. Itoh. 1999. Tying
1248 a molecular knot with optical tweezers. *Nature*. 399:446-448.

1249 Baumgart, F., A.M. Arnold, K. Leskovar, K. Staszek, M. Folser, J. Weghuber, H. Stockinger,
1250 and G.J. Schutz. 2016. Varying label density allows artifact-free analysis of membrane-protein
1251 nanoclusters. *Nat Methods*. 13:661-664.

1252 Behringer, R., M. Gertsenstein, K. Vintersten, and A. Nagy. 2014. Manipulating the Mouse
1253 Embryo: A Laboratory Manual. Cold Spring Harbor Laboratory Press, New York. 814 pp.

1254 Bui, K.H., A. von Appen, A.L. DiGuilio, A. Ori, L. Sparks, M.T. Mackmull, T. Bock, W. Hagen,
1255 A. Andres-Pons, J.S. Glavy, and M. Beck. 2013. Integrated structural analysis of the human
1256 nuclear pore complex scaffold. *Cell*. 155:1233-1243.

1257 Caetano, F.A., B.S. Dirk, J.H. Tam, P.C. Cavanagh, M. Goiko, S.S. Ferguson, S.H. Pasternak,
1258 J.D. Dikeakos, J.R. de Bruyn, and B. Heit. 2015. MIiSR: Molecular Interactions in Super-
1259 Resolution Imaging Enables the Analysis of Protein Interactions, Dynamics and Formation of
1260 Multi-protein Structures. *PLoS Comput Biol*. 11:e1004634.

1261 Chen, Y., L. Zardi, and D.M. Peters. 1997. High-resolution cryo-scanning electron microscopy
1262 study of the macromolecular structure of fibronectin fibrils. *Scanning*. 19:349-355.

1263 Chernousov, M.A., A.I. Faerman, M.G. Frid, O. Printseva, and V.E. Koteliansky. 1987.
1264 Monoclonal antibody to fibronectin which inhibits extracellular matrix assembly. *FEBS Lett*.
1265 217:124-128.

1266 Chiang, H.Y., V.A. Korshunov, A. Serour, F. Shi, and J. Sottile. 2009. Fibronectin is an
1267 important regulator of flow-induced vascular remodeling. *Arterioscler Thromb Vasc Biol*.
1268 29:1074-1079.

1269 Choi, M.G., and R.O. Hynes. 1979. Biosynthesis and processing of fibronectin in NIL.8
1270 hamster cells. *J Biol Chem*. 254:12050-12055.

1271 Diekmann, R., M. Kahnwald, A. Schoenit, J. Deschamps, U. Matti, and J. Ries. 2020.
1272 Optimizing imaging speed and excitation intensity for single-molecule localization microscopy.
1273 *Nat Methods*. 17:909-912.

1274 Dzamba, B.J., and D.M. Peters. 1991. Arrangement of cellular fibronectin in noncollagenous
1275 fibrils in human fibroblast cultures. *J Cell Sci*. 100 (Pt 3):605-612.

1276 Engel, J., E. Odermatt, A. Engel, J.A. Madri, H. Furthmayr, H. Rohde, and R. Timpl. 1981.
1277 Shapes, domain organizations and flexibility of laminin and fibronectin, two multifunctional
1278 proteins of the extracellular matrix. *J Mol Biol*. 150:97-120.

1279 Erickson, H.P., N. Carrell, and J. McDonagh. 1981. Fibronectin molecule visualized in electron
1280 microscopy: a long, thin, flexible strand. *J Cell Biol*. 91:673-678.

1281 Ester, M., H.-P. Krigel, J. Sander, and X. Xu. 1996. A density-based algorithm for discovering
1282 clusters in large spatial databases with noise. *Proc Second Int Conf Knowl Discov Data*
1283 *Min.*:226–231.

1284 Filla, M.S., K.D. Dimeo, T. Tong, and D.M. Peters. 2017. Disruption of fibronectin matrix affects
1285 type IV collagen, fibrillin and laminin deposition into extracellular matrix of human trabecular
1286 meshwork (HTM) cells. *Exp Eye Res*. 165:7-19.

1287 Fruh, S.M., I. Schoen, J. Ries, and V. Vogel. 2015. Molecular architecture of native fibronectin
1288 fibrils. *Nat Commun*. 6:7275.

1289 Furcht, L.T., D. Smith, G. Wendelschafer-Crabb, D.F. Mosher, and J.M. Foidart. 1980a.
1290 Fibronectin presence in native collagen fibrils of human fibroblasts: immunoperoxidase and
1291 immunoferritin localization. *J Histochem Cytochem*. 28:1319-1333.

1292 Furcht, L.T., G. Wendelschafer-Crabb, D.F. Mosher, and J.M. Foidart. 1980b. Ascorbate-
1293 induced fibroblast cell matrix: reaction of antibodies to procollagen I and III and fibronectin in
1294 an axial periodic fashion. *Prog Clin Biol Res*. 41:829-843.

1295 Furcht, L.T., G. Wendelschafer-Crabb, D.F. Mosher, and J.M. Foidart. 1980c. An axial periodic
1296 fibrillar arrangement of antigenic determinants for fibronectin and procollagen on ascorbate
1297 treated human fibroblasts. *J Supramol Struct*. 13:15-33.

1298 Geiger, B., A. Bershadsky, R. Pankov, and K.M. Yamada. 2001. Transmembrane crosstalk
1299 between the extracellular matrix--cytoskeleton crosstalk. *Nature reviews. Molecular cell*
1300 *biology*. 2:793-805.

1301 Geiger, B., and K.M. Yamada. 2011. Molecular architecture and function of matrix adhesions.
1302 *Cold Spring Harb Perspect Biol*. 3.

1303 Gudzenko, T., and C.M. Franz. 2015. Studying early stages of fibronectin fibrillogenesis in
1304 living cells by atomic force microscopy. *Mol Biol Cell*. 26:3190-3204.

1305 Guvendiren, M., and J.A. Burdick. 2012. Stiffening hydrogels to probe short- and long-term
1306 cellular responses to dynamic mechanics. *Nat Commun*. 3:792.

1307 Guvendiren, M., S. Yang, and J.A. Burdick. 2009. Swelling-Induced Surface Patterns in
1308 Hydrogels with Gradient Crosslinking Density. *Advanced Functional Materials*. 19:3038-3045.

1309 Heilemann, M., S. van de Linde, M. Schuttpelz, R. Kasper, B. Seefeldt, A. Mukherjee, P.
1310 Tinnefeld, and M. Sauer. 2008. Subdiffraction-resolution fluorescence imaging with
1311 conventional fluorescent probes. *Angew Chem Int Ed Engl*. 47:6172-6176.

1312 Hocking, D.C., J. Sottile, and P.J. McKeown-Longo. 1994. Fibronectin's III-1 module contains a
1313 conformation-dependent binding site for the amino-terminal region of fibronectin. *J Biol Chem*.
1314 269:19183-19187.

1315 Hynes, R.O. 1990. Fibronectins. Springer-Verlag, New York.

1316 Hynes, R.O. 2009. The extracellular matrix: not just pretty fibrils. *Science*. 326:1216-1219.

1317 Jimenez, A., K. Friedl, and C. Leterrier. 2020. About samples, giving examples: Optimized
1318 Single Molecule Localization Microscopy. *Methods*. 174:100-114.

1319 Kaech, S., and G. Banker. 2006. Culturing hippocampal neurons. *Nat Protoc*. 1:2406-2415.

1320 Khetan, S., M. Guvendiren, W.R. Legant, D.M. Cohen, C.S. Chen, and J.A. Burdick. 2013.
1321 Degradation-mediated cellular traction directs stem cell fate in covalently crosslinked three-
1322 dimensional hydrogels. *Nature Materials*. 12:458-465.

1323 Lansky, Z., Y. Mutsafi, L. Houben, T. Ilani, G. Armony, S.G. Wolf, and D. Fass. 2019. 3D
1324 mapping of native extracellular matrix reveals cellular responses to the microenvironment. *J*
1325 *Struct Biol X*. 1:100002.

1326 Lelek, M., M.T. Gyparaki, G. Beliu, F. Schueder, J. Griffié, S. Manley, R. Jungmann, M. Sauer,
1327 M. Lakadamyali, and C. Zimmer. 2021. Single-molecule localization microscopy. *Nature*
1328 *Reviews Methods Primers*. 1:39.

1329 Lu, J., A.D. Doyle, Y. Shinsato, S. Wang, M.A. Bodendorfer, M. Zheng, and K.M. Yamada.
1330 2020. Basement Membrane Regulates Fibronectin Organization Using Sliding Focal
1331 Adhesions Driven by a Contractile Winch. *Dev Cell*. 52:631-646 e634.

1332 Ma, W., H. Ma, and D.F. Mosher. 2015. On-Off Kinetics of Engagement of FNI Modules of
1333 Soluble Fibronectin by beta-Strand Addition. *PLoS One*. 10:e0124941.

1334 Malkusch, S., U. Endesfelder, J. Mondry, M. Gelleri, P.J. Verveer, and M. Heilemann. 2012.
1335 Coordinate-based colocalization analysis of single-molecule localization microscopy data.
1336 *Histochem Cell Biol*. 137:1-10.

1337 Martino, M.M., and J.A. Hubbell. 2010. The 12th-14th type III repeats of fibronectin function as
1338 a highly promiscuous growth factor-binding domain. *FASEB J*. 24:4711-4721.

1339 Mau, A., K. Friedl, C. Leterrier, N. Bourg, and S. Leveque-Fort. 2021. Fast widefield scan
1340 provides tunable and uniform illumination optimizing super-resolution microscopy on large
1341 fields. *Nat Commun*. 12:3077.

1342 Maurer, L.M., B.R. Tomasini-Johansson, W. Ma, D.S. Annis, N.L. Eickstaedt, M.G.
1343 Ensenberger, K.A. Satyshur, and D.F. Mosher. 2010. Extended binding site on fibronectin for
1344 the functional upstream domain of protein F1 of Streptococcus pyogenes. *J Biol Chem*.
1345 285:41087-41099.

1346 Mautner, V., and R.O. Hynes. 1977. Surface distribution of LETS protein in relation to the
1347 cytoskeleton of normal and transformed cells. *J Cell Biol*. 75:743-768.

1348 McKeown-Longo, P.J., and D.F. Mosher. 1983. Binding of plasma fibronectin to cell layers of
1349 human skin fibroblasts. *J Cell Biol*. 97:466-472.

1350 Morla, A., Z. Zhang, and E. Ruoslahti. 1994. Superfibronectin is a functionally distinct form of
1351 fibronectin. *Nature*. 367:193-196.

1352 Mund, M., and J. Ries. 2020. How good are my data? Reference standards in superresolution
1353 microscopy. *Mol Biol Cell*. 31:2093-2096.

1354 Muzumdar, M.D., B. Tasic, K. Miyamichi, L. Li, and L. Luo. 2007. A global double-fluorescent
1355 Cre reporter mouse. *Genesis*. 45:593-605.

1356 Nieuwenhuizen, R.P., K.A. Lidke, M. Bates, D.L. Puig, D. Grunwald, S. Stallinga, and B.
1357 Rieger. 2013. Measuring image resolution in optical nanoscopy. *Nat Methods*. 10:557-562.

1358 Ohashi, T., D.P. Kiehart, and H.P. Erickson. 1999. Dynamics and elasticity of the fibronectin
1359 matrix in living cell culture visualized by fibronectin-green fluorescent protein. *Proc Natl Acad*
1360 *Sci U S A*. 96:2153-2158.

1361 Ovesny, M., P. Krizek, J. Borkovec, Z. Svindrych, and G.M. Hagen. 2014. ThunderSTORM: a
1362 comprehensive ImageJ plug-in for PALM and STORM data analysis and super-resolution
1363 imaging. *Bioinformatics*. 30:2389-2390.

1364 Pankov, R., E. Cukierman, B.Z. Katz, K. Matsumoto, D.C. Lin, S. Lin, C. Hahn, and K.M.
1365 Yamada. 2000. Integrin dynamics and matrix assembly: tensin-dependent translocation of
1366 alpha(5)beta(1) integrins promotes early fibronectin fibrillogenesis. *J Cell Biol*. 148:1075-1090.

1367 Pankov, R., A. Momchilova, N. Stefanova, and K.M. Yamada. 2019. Characterization of stitch
1368 adhesions: Fibronectin-containing cell-cell contacts formed by fibroblasts. *Exp Cell Res*.
1369 384:111616.

1370 Patla, I., T. Volberg, N. Elad, V. Hirschfeld-Warneken, C. Grashoff, R. Fassler, J.P. Spatz, B.
1371 Geiger, and O. Medalia. 2010. Dissecting the molecular architecture of integrin adhesion sites
1372 by cryo-electron tomography. *Nat Cell Biol*. 12:909-915.

1373 Perez, A.R., Y. Pritykin, J.A. Vidigal, S. Chhangawala, L. Zamparo, C.S. Leslie, and A.
1374 Ventura. 2017. GuideScan software for improved single and paired CRISPR guide RNA
1375 design. *Nat Biotechnol*. 35:347-349.

1376 Peters, D.M., L.M. Portz, J. Fullenwider, and D.F. Mosher. 1990. Co-assembly of plasma and
1377 cellular fibronectins into fibrils in human fibroblast cultures. *J Cell Biol*. 111:249-256.

1378 Peters, J.H., and R.O. Hynes. 1996. Fibronectin isoform distribution in the mouse. I. The
1379 alternatively spliced EIIIB, EIIIA, and V segments show widespread codistribution in the
1380 developing mouse embryo. *Cell Adhes Commun*. 4:103-125.

1381 Pliatsika, V., and I. Rigoutsos. 2015. "Off-Spotter": very fast and exhaustive enumeration of
1382 genomic lookalikes for designing CRISPR/Cas guide RNAs. *Biol Direct*. 10:4.

1383 Raitman, I., M.L. Huang, S.A. Williams, B. Friedman, K. Godula, and J.E. Schwarzbauer. 2018.
1384 Heparin-fibronectin interactions in the development of extracellular matrix insolubility. *Matrix*
1385 *Biol*. 67:107-122.

1386 Ramirez, A., and S. Astrof. 2020. Visualization and Analysis of Pharyngeal Arch Arteries using
1387 Whole-mount Immunohistochemistry and 3D Reconstruction. *J. Vis. Exp.* 157:e60797.

1388 Ran, F.A., P.D. Hsu, J. Wright, V. Agarwala, D.A. Scott, and F. Zhang. 2013. Genome
1389 engineering using the CRISPR-Cas9 system. *Nat Protoc*. 8:2281-2308.

1390 Rickelt, S., and R.O. Hynes. 2018. Antibodies and methods for immunohistochemistry of
1391 extracellular matrix proteins. *Matrix Biol*. 71-72:10-27.

1392 Ries, J. 2020. SMAP: a modular super-resolution microscopy analysis platform for SMLM data.
1393 *Nat Methods*. 17:870-872.

1394 Rozario, T., B. Dzamba, G.F. Weber, L.A. Davidson, and D.W. DeSimone. 2009. The physical
1395 state of fibronectin matrix differentially regulates morphogenetic movements in vivo. *Dev Biol*.
1396 327:386-398.

1397 Rust, M.J., M. Bates, and X. Zhuang. 2006. Sub-diffraction-limit imaging by stochastic optical
1398 reconstruction microscopy (STORM). *Nat Methods*. 3:793-795.

1399 Saitta, A.M., P.D. Soper, E. Wasserman, and M.L. Klein. 1999. Influence of a knot on the
1400 strength of a polymer strand. *Nature*. 399:46-48.

1401 Sakai, T., K.J. Johnson, M. Murozono, K. Sakai, M.A. Magnuson, T. Wieloch, T. Cronberg, A.
1402 Isshiki, H.P. Erickson, and R. Fassler. 2001. Plasma fibronectin supports neuronal survival and
1403 reduces brain injury following transient focal cerebral ischemia but is not essential for skin-
1404 wound healing and hemostasis. *Nat Med*. 7:324-330.

1405 Saunders, J.T., and J.E. Schwarzbauer. 2019. Fibronectin matrix as a scaffold for procollagen
1406 proteinase binding and collagen processing. *Mol Biol Cell*. 30:2218-2226.

1407 Schwarzbauer, J.E. 1991. Identification of the fibronectin sequences required for assembly of a
1408 fibrillar matrix. *J Cell Biol*. 113:1463-1473.

1409 Schwarzbauer, J.E., and D.W. DeSimone. 2011. Fibronectins, their fibrillogenesis, and in vivo
1410 functions. *Cold Spring Harbor perspectives in biology*. 3.

1411 Sechler, J.L., H. Rao, A.M. Cumiskey, I. Vega-Colon, M.S. Smith, T. Murata, and J.E.
1412 Schwarzbauer. 2001. A novel fibronectin binding site required for fibronectin fibril growth
1413 during matrix assembly. *J Cell Biol*. 154:1081-1088.

1414 Sechler, J.L., Y. Takada, and J.E. Schwarzbauer. 1996. Altered rate of fibronectin matrix
1415 assembly by deletion of the first type III repeats. *J Cell Biol*. 134:573-583.

1416 Shaner, N.C., P.A. Steinbach, and R.Y. Tsien. 2005. A guide to choosing fluorescent proteins.
1417 *Nat Methods*. 2:905-909.

1418 Singh, P., C. Carraher, and J.E. Schwarzbauer. 2010. Assembly of fibronectin extracellular
1419 matrix. *Annu Rev Cell Dev Biol*. 26:397-419.

1420 Singh, P., and J.E. Schwarzbauer. 2014. Fibronectin matrix assembly is essential for cell
1421 condensation during chondrogenesis. *J Cell Sci*. 127:4420-4428.

1422 Sivakumar, P., A. Czirok, B.J. Rongish, V.P. Divakara, Y.P. Wang, and S.L. Dallas. 2006. New
1423 insights into extracellular matrix assembly and reorganization from dynamic imaging of
1424 extracellular matrix proteins in living osteoblasts. *J Cell Sci*. 119:1350-1360.

1425 Skorstengaard, K., M.S. Jensen, P. Sahl, T.E. Petersen, and S. Magnusson. 1986. Complete
1426 primary structure of bovine plasma fibronectin. *Eur J Biochem*. 161:441-453.

1427 Smith, M.L., D. Gourdon, W.C. Little, K.E. Kubow, R.A. Eguiluz, S. Luna-Morris, and V. Vogel.
1428 2007. Force-induced unfolding of fibronectin in the extracellular matrix of living cells. *PLoS*
1429 *Biol*. 5:e268.

1430 Snitkovsky, S., and J.A. Young. 1998. Cell-specific viral targeting mediated by a soluble
1431 retroviral receptor-ligand fusion protein. *Proc Natl Acad Sci U S A*. 95:7063-7068.

1432 Sottile, J., and J. Chandler. 2005. Fibronectin matrix turnover occurs through a caveolin-1-
1433 dependent process. *Mol Biol Cell*. 16:757-768.

1434 Thevathasan, J.V., M. Kahnwald, K. Cieslinski, P. Hoess, S.K. Peneti, M. Reitberger, D. Heid,
1435 K.C. Kasuba, S.J. Hoerner, Y. Li, Y.L. Wu, M. Mund, U. Matti, P.M. Pereira, R. Henriques, B.
1436 Nijmeijer, M. Kueblbeck, V.J. Sabinina, J. Ellenberg, and J. Ries. 2019. Nuclear pores as
1437 versatile reference standards for quantitative superresolution microscopy. *Nat Methods*.
1438 16:1045-1053.

1439 Tomasini-Johansson, B.R., D.S. Annis, and D.F. Mosher. 2006. The N-terminal 70-kDa
1440 fragment of fibronectin binds to cell surface fibronectin assembly sites in the absence of intact
1441 fibronectin. *Matrix Biol*. 25:282-293.

1442 Tomasini-Johansson, B.R., N.R. Kaufman, M.G. Ensenberger, V. Ozeri, E. Hanski, and D.F.
1443 Mosher. 2001. A 49-residue peptide from adhesin F1 of Streptococcus pyogenes inhibits
1444 fibronectin matrix assembly. *J Biol Chem*. 276:23430-23439.

1445 von Appen, A., J. Kosinski, L. Sparks, A. Ori, A.L. DiGuilio, B. Vollmer, M.T. Mackmull, N.
1446 Banterle, L. Parca, P. Kastritis, K. Buczak, S. Mosalaganti, W. Hagen, A. Andres-Pons, E.A.
1447 Lemke, P. Bork, W. Antonin, J.S. Glavy, K.H. Bui, and M. Beck. 2015. In situ structural
1448 analysis of the human nuclear pore complex. *Nature*. 526:140-143.

1449 Wagner, D.D., and R.O. Hynes. 1979. Domain structure of fibronectin and its relation to
1450 function. Disulfides and sulfhydryl groups. *J Biol Chem*. 254:6746-6754.

1451 Wierzbicka-Patynowski, I., Y. Mao, and J.E. Schwarzbauer. 2004. Analysis of fibronectin
1452 matrix assembly. *Current protocols in cell biology / editorial board, Juan S. Bonifacino ... [et*
1453 *al.]*. Chapter 10:Unit 10 12.

1454 Wijelath, E.S., J. Murray, S. Rahman, Y. Patel, A. Ishida, K. Strand, S. Aziz, C. Cardona, W.P.
1455 Hammond, G.F. Savidge, S. Rafii, and M. Sobel. 2002. Novel Vascular Endothelial Growth
1456 Factor Binding Domains of Fibronectin Enhance Vascular Endothelial Growth Factor Biological
1457 Activity. *Circulation research*. 91:25-31.

1458 Yuan, L., M. Siegel, K. Choi, C. Khosla, C.R. Miller, E.N. Jackson, D. Piwnica-Worms, and
1459 K.M. Rich. 2007. Transglutaminase 2 inhibitor, KCC009, disrupts fibronectin assembly in the
1460 extracellular matrix and sensitizes orthotopic glioblastomas to chemotherapy. *Oncogene*.
1461 26:2563-2573.

1462 Zamir, E., B.Z. Katz, S. Aota, K.M. Yamada, B. Geiger, and Z. Kam. 1999. Molecular diversity
1463 of cell-matrix adhesions. *J Cell Sci*. 112 (Pt 11):1655-1669.

1464 Zamir, E., M. Katz, Y. Posen, N. Erez, K.M. Yamada, B.Z. Katz, S. Lin, D.C. Lin, A.
1465 Bershadsky, Z. Kam, and B. Geiger. 2000. Dynamics and segregation of cell-matrix adhesions
1466 in cultured fibroblasts. *Nat Cell Biol*. 2:191-196.

1467 Zhang, Q., W.J. Checovich, D.M. Peters, R.M. Albrecht, and D.F. Mosher. 1994. Modulation of
1468 cell surface fibronectin assembly sites by lysophosphatidic acid. *J Cell Biol*. 127:1447-1459.

1469 Zhang, Q., M.K. Magnusson, and D.F. Mosher. 1997. Lysophosphatidic acid and microtubule-
1470 destabilizing agents stimulate fibronectin matrix assembly through Rho-dependent actin stress
1471 fiber formation and cell contraction. *Mol Biol Cell*. 8:1415-1425.

1472 Zhang, Q., and D.F. Mosher. 1996. Cross-linking of the NH2-terminal region of fibronectin to
1473 molecules of large apparent molecular mass. Characterization of fibronectin assembly sites
1474 induced by the treatment of fibroblasts with lysophosphatidic acid. *J Biol Chem*. 271:33284-
1475 33292.

1476 Zhong, C., M. Chrzanowska-Wodnicka, J. Brown, A. Shaub, A.M. Belkin, and K. Burridge.
1477 1998. Rho-mediated contractility exposes a cryptic site in fibronectin and induces fibronectin
1478 matrix assembly. *J Cell Biol*. 141:539-551.

1479 Zhou, X., R.G. Rowe, N. Hiraoka, J.P. George, D. Wirtz, D.F. Mosher, I. Virtanen, M.A.
1480 Chernousov, and S.J. Weiss. 2008. Fibronectin fibrillogenesis regulates three-dimensional
1481 neovessel formation. *Genes Dev*. 22:1231-1243.
1482

Table 1. Effective labeling efficiency and standardized SMLM measurements

Sample	Buffer	ELE (%)	Average # Localizations per NPC	# Localizations per protein	Radius of NPC, nm
U2OS-Nup96	GLOX/BME	79.6+/-5.4	280 +/- 49.2	8.75 +/- 1.54	63.6 +/- 0.86

$NUP96^{mEGFP/mEGFP}$ cells were imaged using αGFP 1° antibody and AF647-conjugated 2° antibody detecting NUP96-mEGFP; SMLM imaging protocol I was used to acquire data. Data is from 3 independent experiments, eight cells, and 4571 NPCs

Table 2 Characterization of Fn1-mEGFP nanodomains in Fn1 fibrils using standardized SMLM protocol

	Buffer	Average PSF (nm)	Average # Localizations per nanodomain	Median Localization Precision, nm	# of mEGFP molecules per nanodomain in Fn1-GFP fibrils	Diameter of Fn1 nanodomain, nm	Nanodomain periodicity, nm
$Fn1^{mEGFP/mEGFP}$ MEFs; αGFP 1° antibody; AF647-conjugated 2° antibody	GLOX/BME	143.8 +/- 2.35	159 +/- 77.92	181	16.85 +/- 5.1	28.26+/-9.7	102±29

αGFP 1° antibody; AF647-conjugated 2° antibody were used to detect Fn1-mEGFP. SMLM imaging protocol I was used to acquire data. Data is from 3 independent experiments, 6 cells, 52 fibrils and 833 nanodomains were used to calculate the number of GFP molecules per nanodomain; To quantify nanodomain dimeter, data from 3 independent experiments, 15 cells, 27 fibrils, and 1292 nanodomains were used.

Figure 1

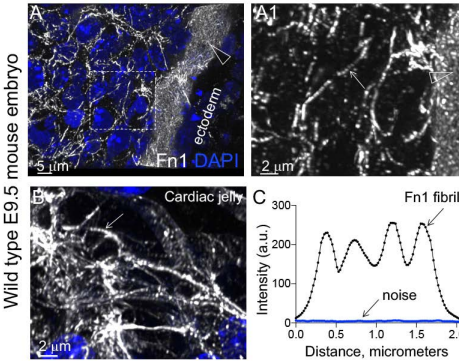

Figure 1. Beaded architecture of Fn1 fibrils in embryonic ECM. Wild-type E9.5 mouse embryos were fixed and stained with the Abcam monoclonal antibody to Fn1 (white) and DAPI (blue), and imaged using 100x oil objective, N.A. 1.49, pinhole 0.8, and sampling rate of 40 nm/pixel. **A – A1.** Sagittal optical section through the first pharyngeal arch and **B.** the cardiac jelly, an ECM-rich region between the myocardial and endocardial layers of the cardiac outflow tract. Large arrowheads in **A – A1** point to the ECM at the ectoderm-mesenchyme boundary of the 1st pharyngeal arch. The box in **(A)** is expanded in **A1** to show Fn1 microarchitecture. Arrow in **A1** points to a beaded Fn1 fibril within the 1st arch mesenchyme; **B.** Beaded architecture of Fn1 fibrils in cardiac jelly, e.g., arrow. **C.** Intensity profile plot of a Fn1 fibril shows a regularly-undulating profile, with troughs well above the background; a.u. arbitrary units.

Figure 2

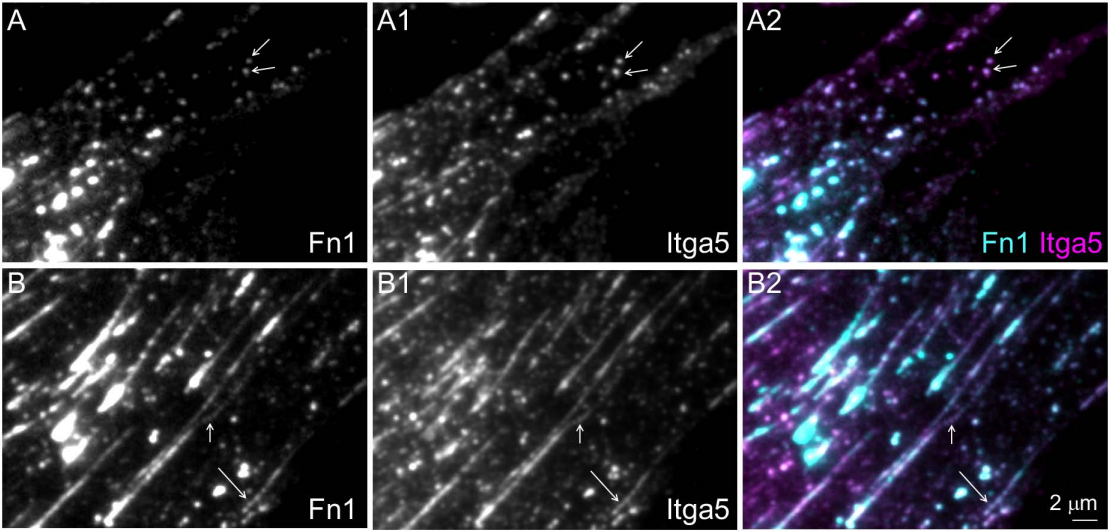

Figure 2. Integrin α5 and Fn1 co-localize in beaded adhesions. Wild-type MEFs were plated for 16 hours on glass coverslips without coating, then fixed, stained with Abcam monoclonal antibodies to Fn1 and anti-integrin α5 (Itga5) antibodies. Cells were imaged at the critical angle of incidence using 100x oil objective, NA 1.49. **A – A2** cell periphery. Arrows in **A-A2** point to examples of non-fibrillar Fn1 adhesions. **B – B2** medial portion of a cell containing beaded fibrillar adhesions (arrows). Magnifications in all panels are the same.

Figure 3

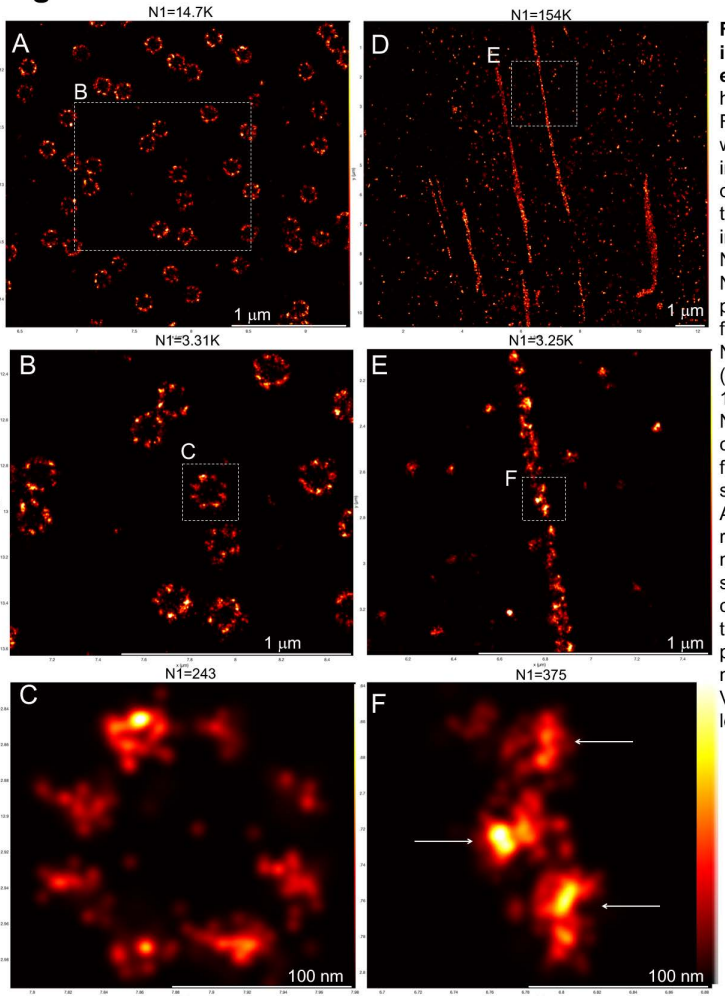

Figure 3. Standardized SMLM imaging results in high resolution and high effective labeling efficiency (ELE). NUP96$^{mEGFP/mEGFP}$ homozygous knock-in cells (**A-C**) and Fn1$^{mEGFP/mEGFP}$ homozygous knock-in cells (**D-F**) were imaged using the same staining and imaging solutions containing anti-GFP 1° at 1:100 dilution and Alexa-647-conjugated 2° antibodies, the same GLOX/BME buffer, and the same imaging protocol (*see Methods*). **A-C.** NUP96$^{mEGFP/mEGFP}$ cells. The distribution of Nup96-mEGFP proteins in the majority of nuclear pore complexes (NPCs) exhibits an expected 8-fold symmetry. See *Table 1* for quantification of NPC dimensions and the ELE. The resolution in (**C**) measured by the Fourier ring curve method is 18.3+/-6.7 nm. **D-F.** Fn1$^{mEGFP/mEGFP}$ cells. Nanodomain architecture of Fn1-mEGFP fibrils is clearly visible in subsequent magnifications of the fibril boxed in (**D**). The boxed region in **D** is shown in **E**. Boxed region in **E** is shown in **F**. Arrows in **F** point to Fn1 nanodomains. The resolution in (**F**) measured by Fourier ring curve method is 14.5+/-1.1 nm. Note that nanodomain size is similar to the size of an NUP96+ NPC corner, which is ~12 nm in actual diameter. N1 is the number of grouped localizations in each panel. See *Table 2* for quantifications of the numbers of mEGFP molecules per nanodomain. Vertical bar in **F** shows color-coding according to localization density for all panels in this figure.

Figure 4

A Schematic of an Fn1 dimer

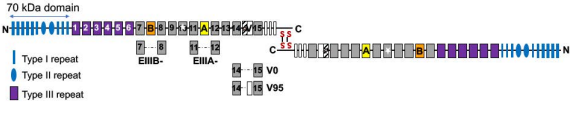

B Antibodies used in these studies and their epitopes

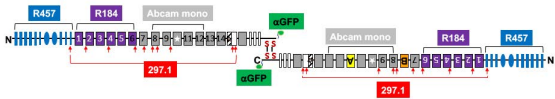

Figure 4. Schematic representations of Fn1 dimers and antibody binding sites. A. Fn1 is secreted as a dimer. Two disulfide bonds at the C-terminus hold Fn1 molecules in an anti-parallel orientation. 70 kDA Fn1 assembly domain is marked in blue and by a double-headed arrow. Fn1 type III repeats are numbered. Splice variants characterized in mice are shown. **B.** Schematic of binding sites for the antibodies used in this manuscript. All antibodies except one are polyclonal, see *Table M2* in the Methods section. Arrows mark mapped epitopes. Brackets mark regions of Fn1 recognized by the following antibodies: R457 is a rabbit polyclonal antibody raised to the 70 kDA domain of Fn1; R184 is a rabbit polyclonal raised against the first six type III repeats of Fn1 (purple); 297.1 is a rabbit polyclonal antibody raised to the full length rat plasma Fn1; The binding sites of 297.1 (red arrows) were mapped in this study (see **Sup. Fig. 4**); Abcam mono is a monoclonal antibody recognizing an epitope within the marked region. αGFP is a polyclonal antibody raised to GFP.

Figure 5

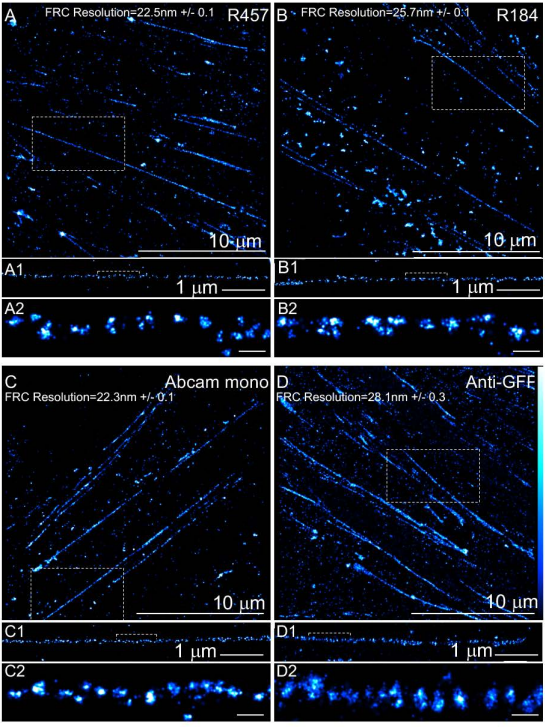

Figure 5. Nanodomain architecture of Fn1 fibrils detected with four different antibodies. Fn1$^{mEGFP/mEGFP}$ MEFs were plated on glass cover slips without coating, cultured over night, and stained with the following antibodies: **A.** R457 (1:200 dilution). **B**. R184 (1:100 dilution). **C**. Abcam monoclonal antibody (1:200 dilution). **D**. anti-GFP antibody (1:100 dilution). Boxes in **A, B, C,** and **D** are expanded to show fibrils in **A1, B1, C1**, and **D1**, respectively. Brackets in **A1, B1, C1,** and **D1** are expanded in **A2, B2, C2**, and **D2**, respectively. Scale bars in **A2, B2, C2**, and **D2** are 100 nm. Fourier ring correlation (FRC) was used to determine image resolution. Vertical bar in **D** shows color-coding according to localization density for all panels in this figure.

Figure 6

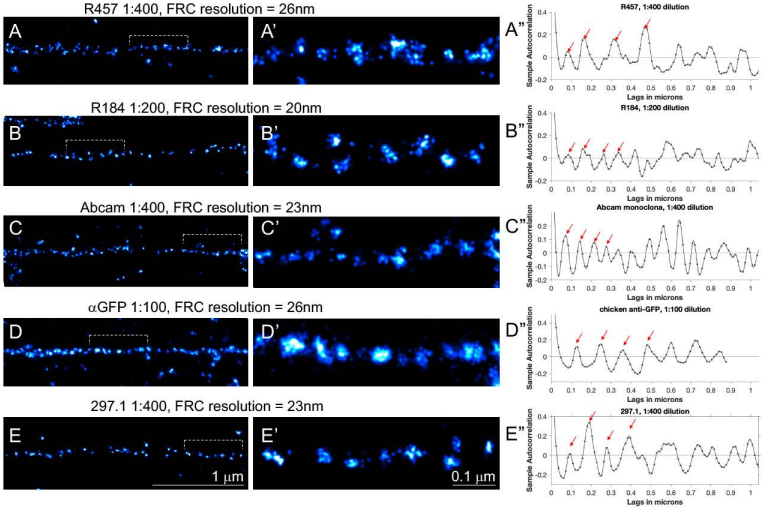

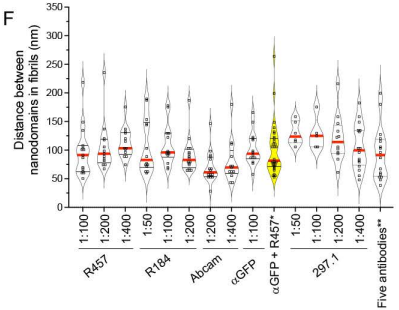

Figure 6. Periodical labeling of Fn1 fibrils by multiple antibodies, their dilutions and combinations. Fn1$^{mEGFP/mEGFP}$ MEFs were plated on glass cover slips without coating, cultured over night, and stained with antibodies indicated. **A-E.** SMLM images resulting from the highest dilutions of antibodies tested. Brackets in **A – E** are expanded in **A'-E'. A''-E''** Autocorrelation traces for fibrils shown in **A-E.** Ljung-Box Q-test for autocorrelation at the peak positions marked by the red arrows resulted in h=1, p=0 indicating strong evidence of autocorrelation at least up to the 4th peak; h (the null hypothesis for this test) is that the first 4 autocorrelations are jointly zero. $h=1$ rejects this hypothesis. **F.** Summary of autocorrelation analyses of multiple fibrils (each fibrils analyzed is marked by a square) stained with different antibody dilutions, and combinations of antibodies. Experiments for each antibody dilution were repeated three independent times, and each time, at least three cells were imaged. One-way ANOVA test with Tukey's correction for multiple testing showed no significant differences among the means. FRC-Fourier ring correlation was used to determine image resolution. * αGFP and R457 were both used at 1:100 dilution. ** The 5 antibodies used and their dilutions were the following: R457(1:400), R184(1:200), Abcam (1:400), αGFP (1:100), 297.1(1:400).

Figure 7

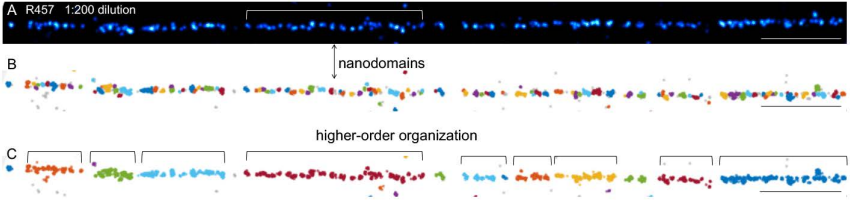

Figure 7. Clustering using DBSCAN suggests a higher-order organization of Fn1 nanodomains in fibrils. Fn1$^{mEGFP/mEGFP}$ MEFs were plated on glass cover slips without coating, cultured over night, and stained with the R457 antibody. The fibril in **A** was analyzed by DBSCAN clustering in **B** and **C**. The minimum number of points per neighborhood (k) was set to 4, as recommended for all 2-dimentional datasets. **B.** The size of the neighborhood, ε, was set to 14 nm, which is an apparent average radius of Fn1 nanodomain (*Table 2*). Adjacent clusters are labeled with different colors. **C**. ε was estimated automatically by the DBSCAN algorithm. Localizations in the same cluster are given the same color; Adjacent clusters are labeled with different colors. DBSCAN clustering in **B** using ε=14 nm discovers Fn1 nanodomains (compare **B** with SMLM image in **A**). Clustering in **C** using an unbiased estimate of ε suggests a higher-order organization of Fn1 nanodomains. Scale bar is 1 micron.

Figure 8

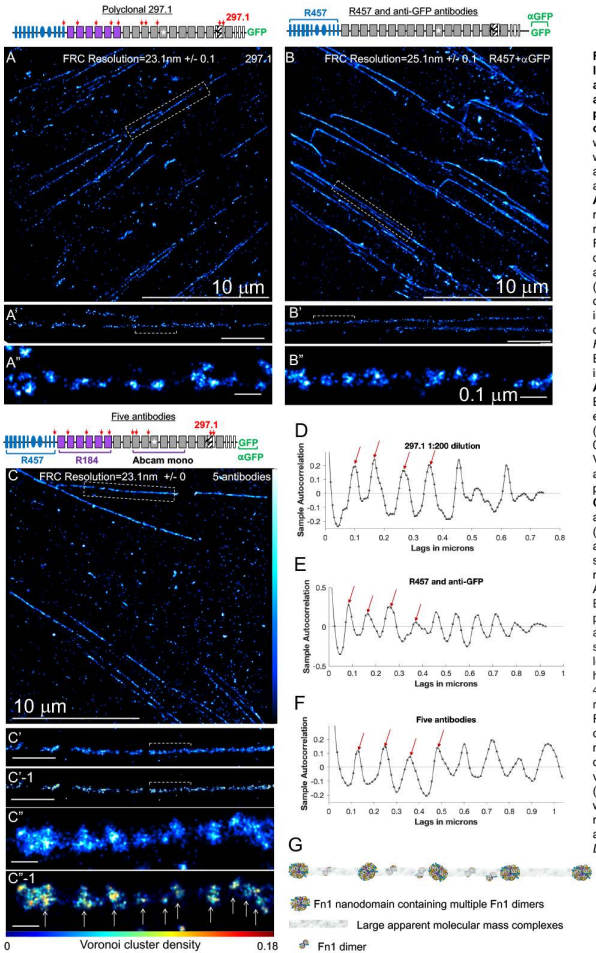

Figure 8 Polyclonal antibody to full-length Fn1 and combinations of antibodies recognizing epitopes along the length of Fn1 reveal periodical nanodomain architecture of Fn1 fibrils. Fn1$^{mEGFP/mEGFP}$ MEFs were plated on glass cover slips without coating, cultured over night, and stained with the indicated antibodies.

A. 297.1 rabbit polyclonal antibody raised to full-length, rat plasma Fn1 recognizing multiple epitopes along Fn1 molecule (red arrows), 1:200 dilution. **B.** A combination of anti-GFP antibody (1:100) and R457 antibody (1:100). **C.** Staining using a combination of 5 antibodies depicted in a schematic above the panel. For dilutions of 5 antibodies see legend to *Fig. 6F*.

Boxed fibrils in **A, B, C** are expanded in **A', B', C'** and **C'-1** (scale bars in **A',B',C'**, and **C'-1** are 1 µm). Bracketed regions in **A', B', C'** are expanded in **A'', B'', C''** and **C'-1** (scale bars in **A'', B'', C''** and **C''-1** are 0.1 µm). **C'-1** and **C''-1**.

Vertical bar in **C** shows color-coding according to localization density for all panels in this figure, except **C'-1** and **C''-1**. **C'-1** and **C''-1** are color-coded according to Voronoi cluster density (horizontal bar below **C''-1**); Clustering analysis based on Voronoi tessellation segments clusters corresponding with nanodomains (arrows in **C''-1**). **D – F.** Autocorrelation analysis and Ljung-Box Q-test for autocorrelation at the peak positions marked by the red arrows resulted in h=1, p=0 indicating strong evidence for autocorrelation at least for the 4 peaks; h (the null hypothesis for this test) is that the first 4 autocorrelations are jointly zero. h=1 rejects this hypothesis. **G.** A model of Fn1 fibril. In this model Fn1 fibrils are composed of periodically-spaced nanodomains containing multiple Fn1 dimers. Nanodomains may be linked via large molecular mass complexes (LAMMs, Zhang and Mosher, 1996) with a few Fn1 dimers between the nanodomains. For additional/alternative models see *Discussion* and *Sup. Fig. 8F1-F2.*

Figure 9

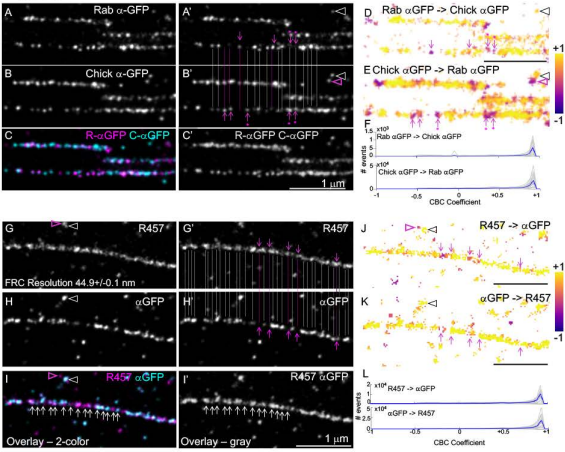

Figure 9. Double-color dSTORM shows that N- and C-termini of Fn1 overlap within Fn1 nanodomains. Fn1$^{mEGFP/mEGFP}$ cells were plated on glass without coating and stained. **A – F.** Control staining. Cells were stained using polyclonal rabbit and chicken anti-GFP antibodies (anti-rabbit 2º antibodies were conjugated to CF680 and anti-chicken 2º antibodies were conjugated to AF640). Panels **A-B** were also displayed as **A'-B'** with vertical lines marking overlapping (gray lines) and non-overlapping (pink lines and arrows) nanodomains; asterisks mark nanodomains in which the signal in one channel is brighter than in the other; **C.** Overlap of two channels in color and **C'** in gray-scale. Less than100% overlap is expected since ELE < 100%. **D-E.** Localizations in **A-B** are color-coded according to the coordinate-based colocalization (CBC) analysis (R_{max}=300, r=30). +1: overlap; ≤ 0: no overlap. Clear arrowheads in **A' , B', D,** and **E** point to an overlapping staining, and pink arrowheads point to an adjacent non-overlapping staining. Pink arrows and asterisks in **A'-B'** are carried over to **D** and **E**, respectively to point non-overlapping staining in fibrils. Asterisks under arrows marks those nanodomains in which the signal in one channel is higher than in the other, but otherwise they co-localize. **F.** CBC coefficients for 22 regions containing long fibrils (gray traces) and their average (blue trace) are plotted. **G-L.** Fn1$^{mEGFP/mEGFP}$ cells were stained using rabbit polyclonal R457 antibody (N-terminus of Fn1) and chicken anti-GFP antibody (C-terminus of Fn1-mEGFP), 2º antibodies were as in **A-F**. **G-H** were duplicated as **G'-H'** with gray lines indicating co-localizing staining and pink lines pointing to non-colocalizing staining. **I - I'** show merged signals for the two antibodies in color (**I**) and gray scale (**I'**). Arrows in **I-I'** point to nanodomains. White and pink arrowheads in **G-I** also show overlapping and non-overlapping staining, respectively. **J-K.** Images in **G-H** are color-coded according to the (CBC) coefficient, (R_{max}=300nm, r=30 nm). Pink arrows in **G'-H'** correspond with pink arrows in **J-K,** respectively. Asterisk under the arrow marks the nanodomains in which the signal in **H'** is higher than in **G'**, but otherwise they co-localize. Note that the CBC analyses distinguish overlapping and non-overlapping localizations in adjacent nanodomains. **L**. CBC coefficients for 20 regions containing long fibrils (gray traces) and their average (blue trace) are plotted, showing a high probability of a near complete overlap between the N- and C- termini of Fn1. Magnifications are the same in all panels. All scale bars are 1 µm. For additional CBC analyses (R_{max}=50nm, r=5nm) see **Sup. Fig. 10.**

Figure 10

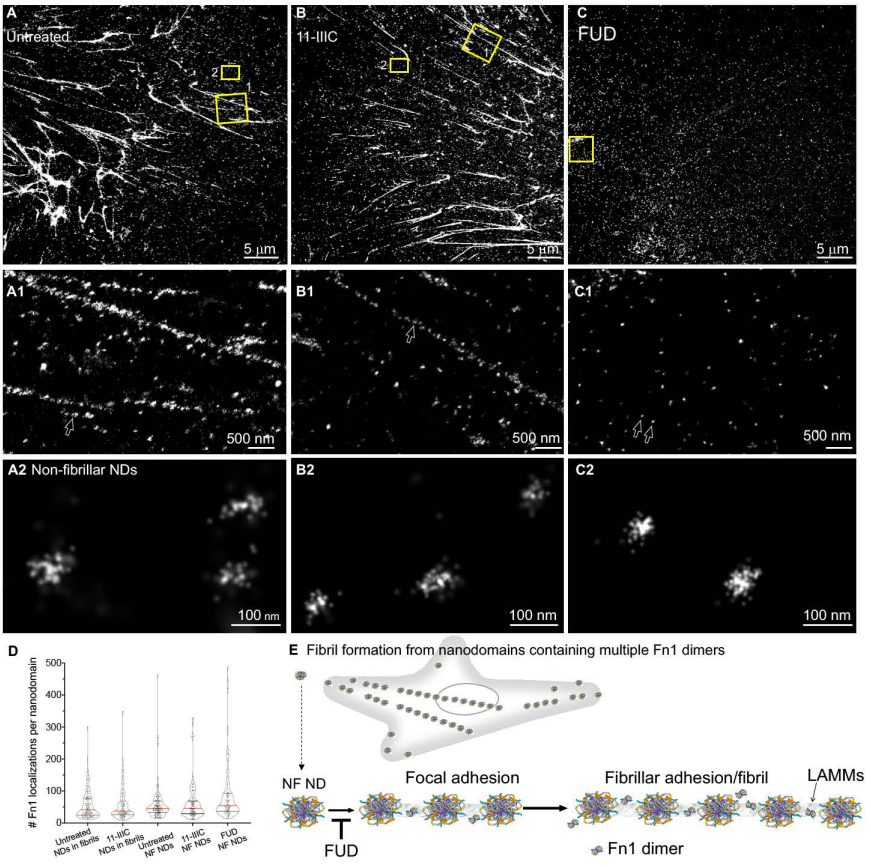

Figure 10. The N-terminal Fn1 assembly domain regulates the organization of Fn1 nanodomains into linear fibrillar arrays. Fn1$^{mEGFP/+}$ MEFs were plated on glass and were either left untreated (**A-A2**), incubated with the control 11-IIIC peptide (**B-B2**), or the FUD peptide (**C-C2**) for 16 hrs. Cells were then washed with PBS, fixed and stained with the Abcam monoclonal antibody to Fn1 followed by Alexa 647-conjugated secondary antibodies. Cells were imaged at the critical angle of incidence by dSTORM. **A – A2**. Untreated, non-permeabilized cells. **B – B2.** Cells incubated with control 11-IIIC peptide, non-permeabilized. **C – C2.** FUD-treated, non-permeabilized cells. Boxes marked 1 in **A-B** are expanded in **A1-B1**. Boxes marked 2 in **A-B**, are expanded in **A2 – B2**. The box in **C** is expanded in **C1** and **C2**. Arrows in **A1-B1** point to Fn1 nanodomains (NDs) in fibrils. Arrows in **C1** point to non-fibrillar (NF) nanodomains expanded in **C2**; **D.** Quantification of the number of grouped Fn1 localizations in nanodomains in fibrils and in non-fibrillar nanodomains after various conditions. Red lines mark medians. Differences are not statistically significant, Kruskal-Wallis test with Dunn's correction for multiple testing. Cells from all experimental conditions were imaged using identical conditions and high laser power (see SMLM imaging protocol II in Methods) explaining lower average number of grouped localizations per nanodomain. **E.** Model of fibril formation in a cell: 6-11 Fn1 dimers assemble into nanodomains containing integrin $\alpha5\beta1$ at cell periphery, move rearward with actin flow, and become organized into linear arrays of nanodomains. Nanodomain arrays are bone fide fibrils. Joining of the additional Fn1 nanodomains to these arrays leads to the generation of longer fibrils as assemblies move toward the cell center. FUD does not interfere with the formation of Fn1 nanodomains; Instead, it blocks the organization of Fn1 nanodomains into linear arrays. LAMMs – large apparent molecular mass complexes, defined in Zhang et al., 1996.

Supplemental Figure 1

A *Fn1* genomic locus near the 3' end of the gene

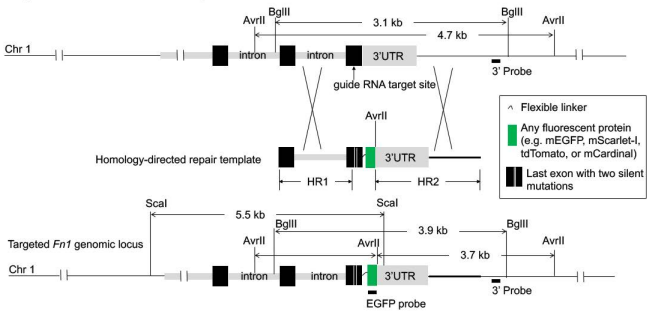

B

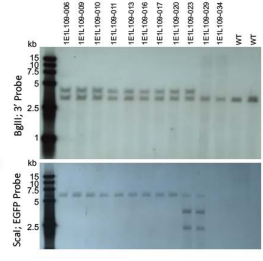

Southern blot strategy			
Restriction enzyme	Probe	WT	Targeted
ScaI	EGFP Probe(5')	--	5.5kb
AvrII	3'Probe	4.7kb	3.7kb
BglII	3'Probe	3.1kb	3.9kb

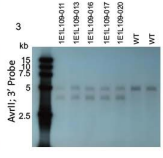

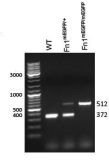

5

Fn1mEGFP/mEGFP x Fn1mEGFP/+ n=22	
Fn1mEGFP/+	Fn1mEGFP/mEGFP
12	10

Supplemental Figure 1. Construction of Fn1^{mEGFP} allele. A. Targeting construct. **B1-B3**. Southern blots. **B1.** Southern blot with 3' probe after digestion with Bgl II. **B2.** Southern blot with GFP probe after digestion with Sca I. **B3.** Southern blot with 3' probe after digestion with AvrII. **B4.** Diagnostic PCR detecting Fn1$^{+/+}$; Fn1$^{mEGFP/+}$; and Fn1$^{mEGFP/mEGFP}$. **B5.** Fn1$^{mEGFP/mEGFP}$ mice are obtained at a Mendelian ratio in the cross between Fn1$^{mEGFP/mEGFP}$ and Fn1$^{mEGFP/+}$ mice.

Supplemental Figure 2

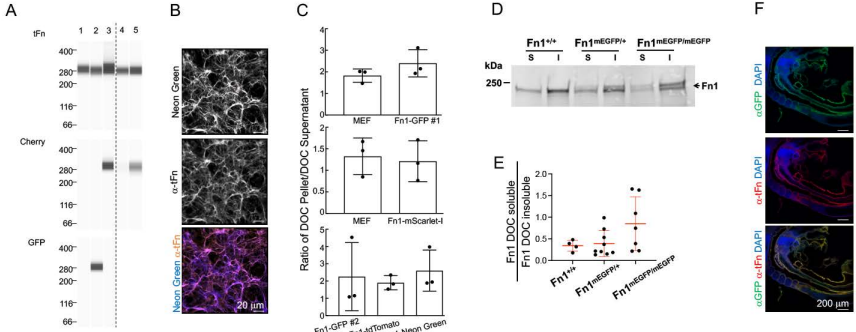

Supplemental Figure 2. Fn1-FP fusion proteins behave like wild-type Fn1 in biochemical assays and *in vivo*. CRISPR was used to knock-in mEGFP, tdTomato, mNeonGreen, or mScarlet-I at the 3' of Fn1 replacing the termination codon in MEFs (see Sup. Fig. 1). **A.** Western blot of cell extracts: 1) wild-type MEFs, 2) $Fn1^{mEGFP}$ MEFs, 3) $Fn1^{tdTomato}$ MEFs, 4) wild-type MEFs, 5) $Fn1^{mScarlet-I}$ MEFs. **B.** $Fn1^{mNeonGreen}$ MEFs were stained with antibody to total Fn1; Native mNeonGreen fluorescence of Fn1-mNeonGreen proteins co-localizes with Abcam monoclonal antibody to tFn1. **C.** Fn1-FP fusion proteins behave like wild-type in DOC matrix assembly assays. **D-E**. Fn1-mEGFP proteins extracted from E9.5 embryos behave like wild-type in DOC matrix assembly assay. **D.** E9.5 embryos were solubilized using DOC lysis buffer and DOC-soluble and insoluble fractions were resolved on a 4-12% SDS-PAGE gel followed by a Western blot using Abcam monoclonal anti-Fn1 antibody. **E**. Quantification of the fraction of Fn1 DOC-soluble Fn1 to DOC-insoluble Fn1. Each dot is an embryo. One-way ANOVA analysis showed no statistical differences between samples from different genotypes. **F.** E9.5 $Fn1^{mEGFP/+}$ embryos were stained with Abcam monoclonal antibody to Fn1 and anti-GFP antibody to detect Fn1 and GFP proteins; Fn1-mEGFP and Fn1 co-localize and are expressed in the expected pattern.

Supplemental Figure 3

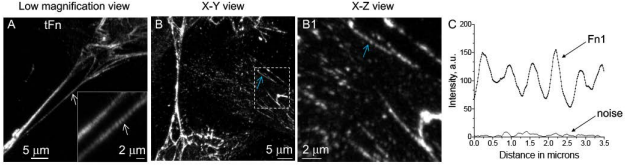

Supplemental Figure 3. Beaded architecture of Fn1 visualized by Zeiss Airyscan. Wild-type MEFs were plated for 48 hours on gelatin-coated glass, fixed and stained to detect Fn1 using the Abcam monoclonal anti-Fn1 antibody, and imaged with the Airyscan modality on Zeiss confocal microscope. **A.** Arrow points to a Fn1 fibril between cells, magnified in the inset. Note the beaded appearance of this fibril, arrows in **A**. Box in **B** is expanded in **B1** and rotated to show the x-z axis, blue arrow points to a beaded fibrillar adhesion. **C.** Intensity profile of the Fn1 fibril marked by the blue arrows in **B** and **B1**. Panel **C** shows that Fn1 fibrils consist of regions of high and low fluorescence intensity.

Supplemental Figure 4

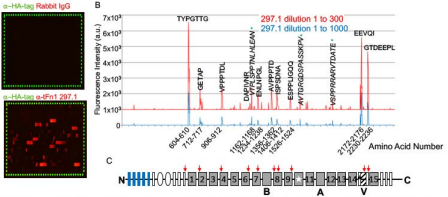

Supplemental Figure 4. 297.1 antibody recognizes multiple epitopes along the Fn1 molecule. A. Custom-prepared peptide arrays fabricated to contained 15-amino acid peptides with 13-amino acid peptide-peptide overlap, spanning the entire mouse Fn1 sequence. HA-tag peptides were spotted around the perimeter for control purposes. Arrays were incubated with anti-HA-tag antibodies followed by the appropriate secondary antibody (green) and with either rabbit IgG (top panel) or 297.1 antibodies (bottom panel) and the appropriate secondaries, red. **B.** Multiple strong to very strong antibody responses against epitope-like spot patterns formed by adjacent peptides with the consensus motifs annotated in the intensity plot at high signal-to-noise ratios; We also observed a few atypical interactions with peptide as highlighted in *italics and marked by asterisks*. Amino acid positions of epitopes are marked on the x-axis. **C.** Positions of 297.1 epitope-binding sites are mapped on mouse Fn1 molecule. The splicing of the V region is depicted according to the mouse mRNA tracks in GENCODE VM27.

Supplemental Figure 5

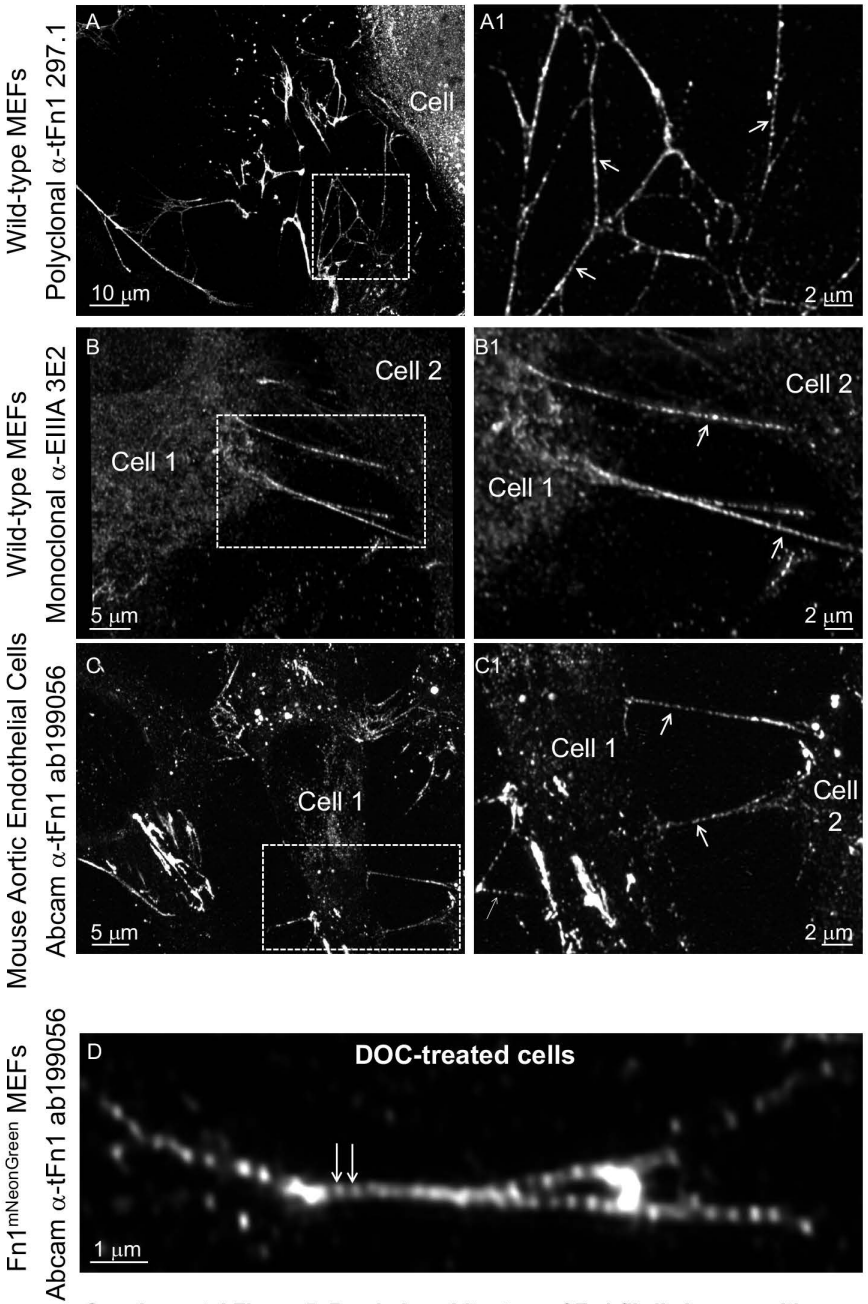

Supplemental Figure 5. Beaded architecture of Fn1 fibrils is seen with multiple antibodies, in different cell types, and is retained in the absence of cell contact. Cells were plated on glass without coating. **A –B.** Fn1 secreted by wild-type MEFs and deposited **A)** on glass or **B)** located between two cells. **C.** Fn1 fibrils between endothelial cells. Boxes in **A – C** are magnified in **A1-C1**. Arrows point to fibrils deposited in the intercellular space (**A1-C1**). **D.** Fn1 fibril imaged following the treatment with 2% deoxycholate for 10 minutes, and staining with Abcam monoclonal antibody to Fn1. Note the beaded architecture of long Fn1 fibril (arrows). Solubilization of cell components by this treatment is shown in **Movie 3**. All images were collected using 100x oil objective, NA 1.49, pinhole size 0.8 Airy units, and sampling resolution of 40 nm/pixel in x,y.

Supplemental Figure 6

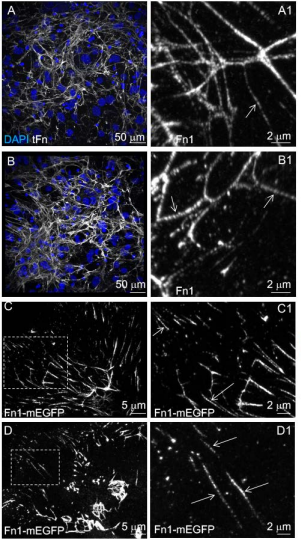

Supplemental Figure 6. Beaded architecture of Fn1 fibrils is observed when cells are plated on different substrata. **A-A1**. Wild-type MEFs plated on laminin-111 for 48 hrs. **B-B1.** Wild-type MEFs plated on vitronectin for 48 hrs. Cells in **A-A1, B-B1** were stained using Abcam monoclonal anti-Fn1 antibody. **A-B.** Low magnification images were recorded with 40x oil objective, **A1-B1.** High magnification images were captured using 100x oil objective, NA 1.49; pinhole was set to 0.8 Airy units, and sampling was done at 40 nm/pixel in x,y (See Methods). **C-D.** Fn1$^{mEGFP/+}$ MEFs were plated for 16 hours on hydrogels derivatized with GRGDSPC peptides (See Methods). Native mEGFP fluorescence was imaged using 100x oil objective, NA 1.49, pinhole size 0.8, and sampling at 40 nm/pixel in x,y). **C – C1.** 3 kPa hydrogel; **D – D1** 12 kPa hydrogel. Arrows point to examples of beaded fibrils.

Supplemental Figure 7

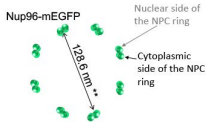

Supplemental Figure 7. Nucleopore complex schematic and diameter measured using anti-GFP antibodies. NPC contains 32 copies of NUP96 protein arranged with an 8-fold symmetry. 16 copies of NUP96 face the cytoplasm, and 16 face the nucleoplasm. **The radius of NPCs measured using NUP96-mEGFP and anti-GFP primary and Alexa-Fluor647-labeled secondary antibodies is 64.3+/-2.6 nm (Thevasian et al., 2019)

Sup. Figure 8

A Model proposed by Dzamba et al., 1991: Fibrils form by extended Fn1 dimers aligned in a periodical manner with regions containing N- termini alternating with regions containing C- termini. Green tail at the C-terminus represents mEGFP

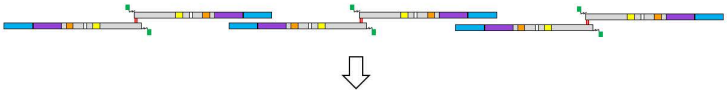

B Dzamba et al., 1991 model posits that periodical alignment of extended Fn1 dimers results in periodical staining pattern of Fn1 fibrils by domain-specific antibodies (Y) in EM images (adopted from Fig. 4A in Dzamba et al., 1991)

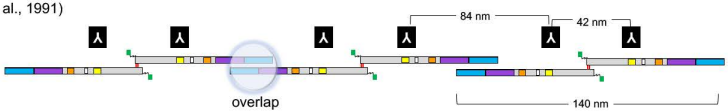

Dotted appearance of Fn1 fibrils seen by immunoelectron microscopy is due to the periodical distribution of region-specific epitopes along the extended Fn1 molecules in a fibril (inverted Y represents a bound antibody)

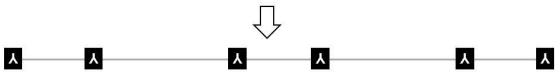

C Dzamba et al., 1991 model predicts that labeling of Fn1 fibrils by the five antibodies depicted below would produce uniformly-labeled fibrils

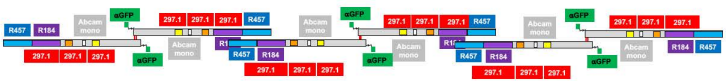

If all of the antibodies in the 5-antibody cocktails are detected with the same color, a fairly-uniform labeling of Fn1 fibrils would be expected according to the model of Dzamba et al., 1991 and Fruh et al., 2015

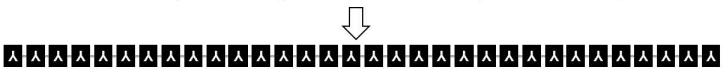

D Canonical model predicts that FUD peptide disrupts Fn1 fibrillogenesis by binding to the N-terminal assembly domain of Fn1 and disrupting the binding between Fn1 dimers:

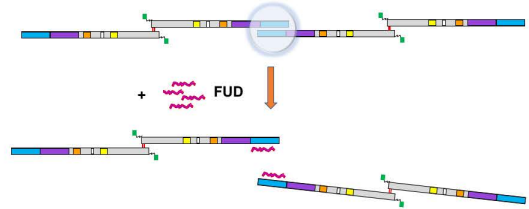

E Biochemical data is also consistent with a model wherein FUD peptides disrupt Fn1 fibrillogenesis by binding to the N-terminal assembly domain of Fn1 and disrupting the binding between Fn1 and a complex containing large apparent molecular mass molecules (LAMMs). This model is based on Zang and Mosher, JBC 1996, and Tomasini et al., Matrix Biology 2006:

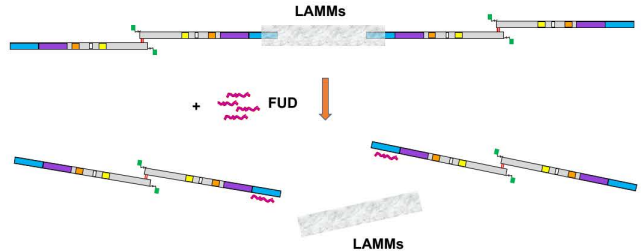

F Models based on the studies in this manuscript

F1 Fn1 nanodomains in fibrils are connected via LAMMs, a few Fn1 dimers are localized between nanodomains

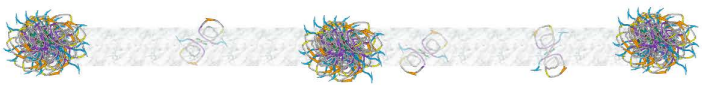

F2 Fn1 nanodomains in fibrils are linked via extended Fn1 dimers

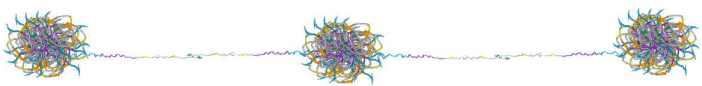

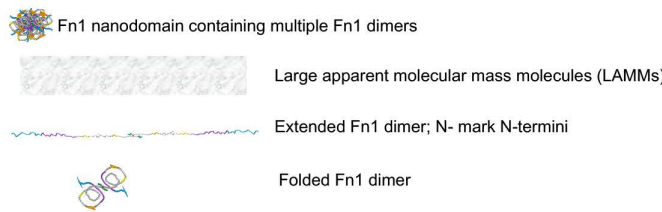

Supplemental Figure 9

Wild-type MEFs | Fn1$^{mEGFP/+}$ MEFs

1 αFn1 III$_{1-6}$, R184 | 2 αFn1 monoclonal | 3 αFn1 297.1 | 4 αFn1 monoclonal | 5 αFn1 monoclonal | 6 αGFP | 7 Antibody cocktail | 8 αFn1 monoclonal

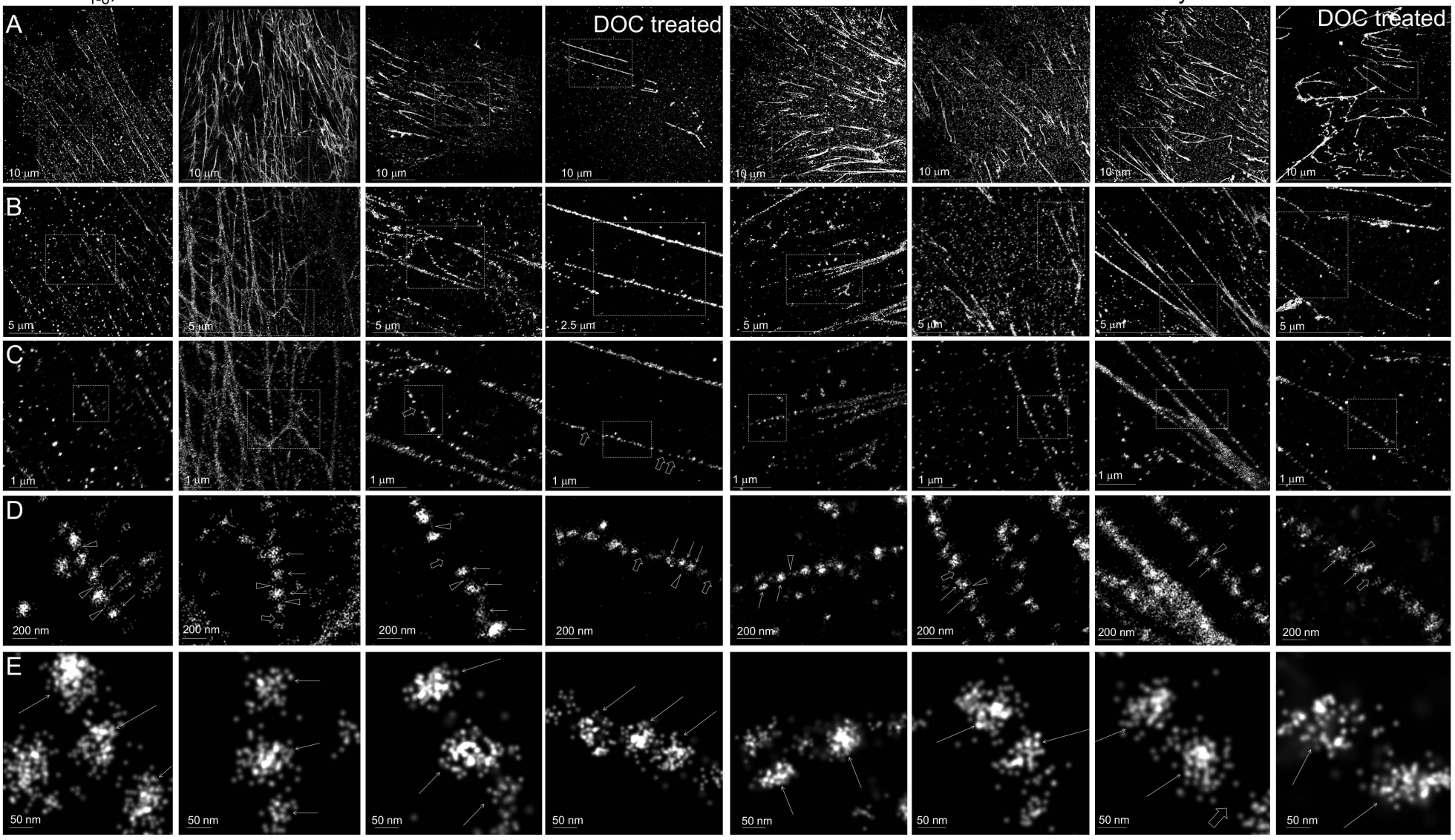

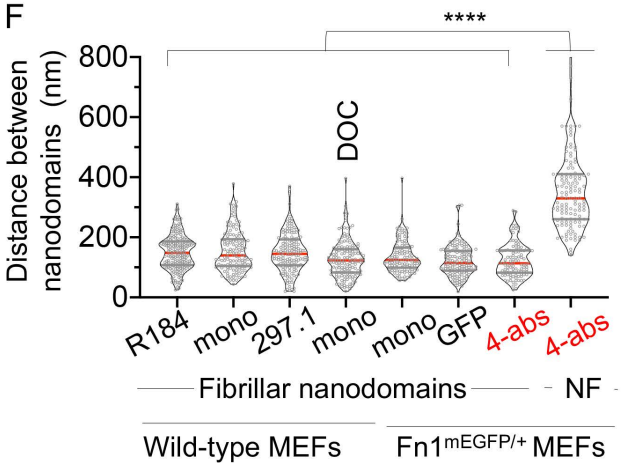

Supplemental Figure 9. Wild-type or Fn1$^{mEGFP/+}$ MEFs were plated on glass for 16 hrs, fixed and stained with different antibodies to Fn1 followed by Alexa 647-conjugated secondary antibodies. Columns 4 and 8 show cells treated with 2% DOC prior to fixation. Cells were imaged using SMLM imaging protocol II**. A.** zoom-out views to show the overall appearance of Fn1 fibrils. **B-E.** Successive magnifications of fibrils shown in row (**A**). Arrows in **D** point to nanodomains magnified in **E;** arrowheads in **D-E** point to Fn1 localizations between nanodomains, wide open arrows point to Fn1-free zones between nanodomains in a fibril. **F.** distances between nanodomains within fibrils or non-fibrillar (NF) nanodomains, **** $p<10^{-4}$, Kruskal-Wallis test, with Dunn's correction for multiple testing. Please note that nanodomain sizes appear larger in these images than in Fig. 5 – 8 because the resolution was lower due to the use of high laser power during bleaching and imaging steps, and the 3D acquisition; FRC-measured resolution in these images ranged between 40-50 nm. Antibody cocktail contained: R184 (1:50), Abcam mono (1:300), 297.1 (1:100) and anti-GFP (1:300) antibodies.

Supplementary Figure 10

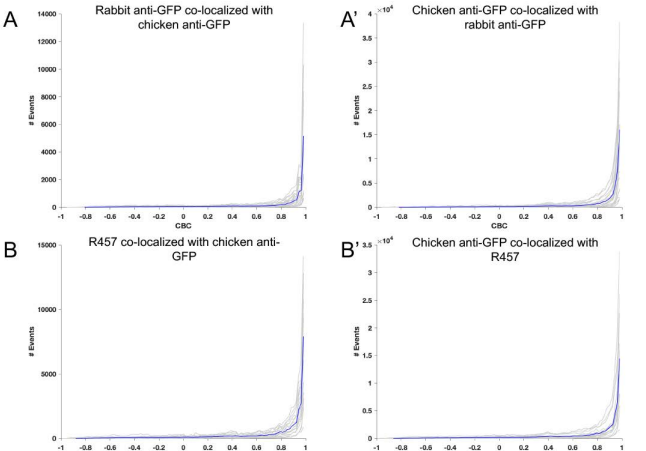

Supplementary Figure 10 CBC analyses show a near complete colocalization of Fn1 N-terminal and C-terminal domains. Cells, plating and staining were as described in **Fig. 9**. CBC analyses were done using ThunderSTORM, R_{max} was set to 50 nm, number of steps was set to 10 (r=5 nm). Blue curve is the average of gray curves. For GFPGFP experiments (**A-A'**), 22 images from 4 cells were analyzed; For R457GFP experiments (**B-B'**), 17 images from 4 cells were analyzed. +1 indicates a high probability of co-localization, ≤ 0 absence of co-localization.

Supplemental Figure 11

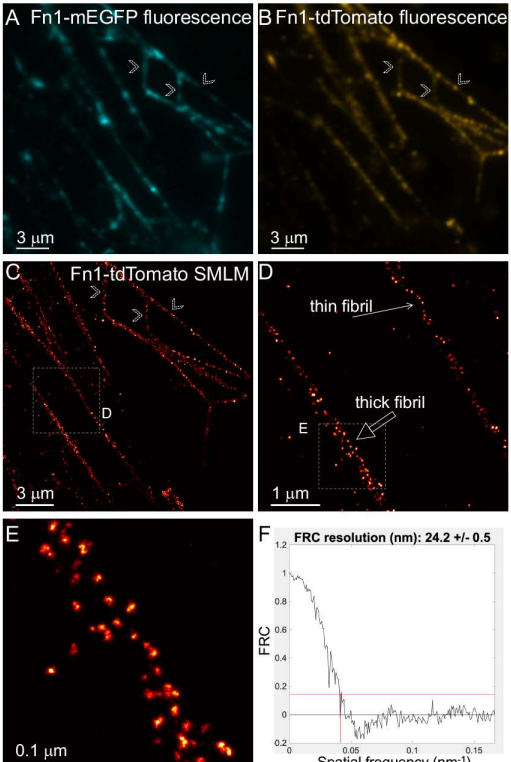

Supplemental Figure 11. Ectopically-added Fn1-tdTomato co-assembles with endogenous Fn1-mEGFP fibrils and forms nanodomains. $Fn1^{mEGFP/mEGFP}$ MEFs were plated on glass without coating at 50% confluency for 16 hours and then incubated with 10 μg of Fn1-tdTomato for 24 hours. Cells were then fixed and stained with rabbit anti-Cherry antibody, which was detected with secondary antibodies conjugated with Alexa-647. Fn1 ECM deposited between cells was imaged. **A – B.** Widefield images taken with 100X Objective, NA 1.49. **A.** Fn1-mEGFP fluorescence. **B.** Fn1-tdTomato fluorescence. **C – E.** dSTORM using SMLM protocol I. **C.** dSTORM image of the region shown in **B.** Examples of fibrils in **C** corresponding with fibrils in the wide-field images (**A-B**) are marked with chevrons. **D.** Magnified region containing a thick and a thin fibril seen in **C. E.** Nanodomain architecture of the thick fibril region boxed in **D.** Note nanodomain architecture of ectopically-added Fn1-tdTomato. **C-E** SMLM images were reconstructed using SMAP (see Methods). **F.** Fourier ring correlation (FRC) analysis performed in SMAP. FRC curve shows the decay of correlation with increasing spatial frequency. Pink line marks the threshold value of 0.143 calculated for SMLM data (Nieuwenhuizen et al., 2013). Red line marks the spatial frequency for which the threshold falls below the value of 0.143. Resolution is calculated as the inverse of the spatial frequency. Resolution of the region shown in **E** is 24.2+/-0.5 nm.

Supplemental Figure 12

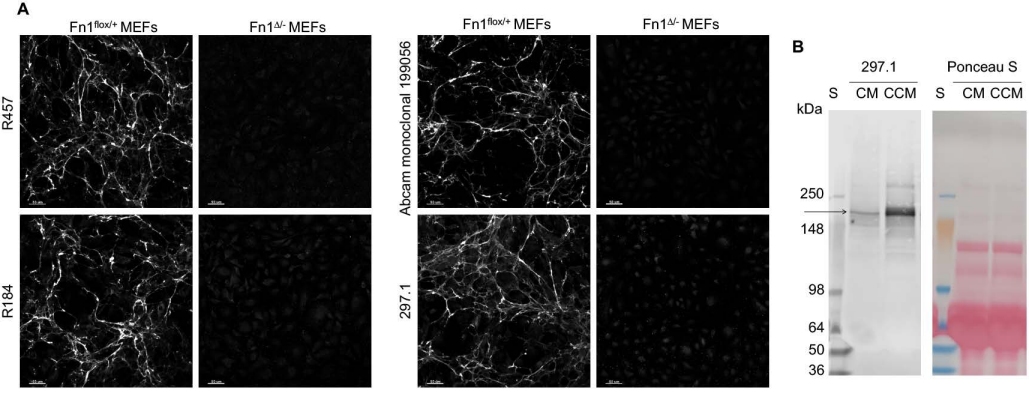

Supplemental Figure 12. Antibodies utilized in this study are specific to fibronectin. A. MEFs were isolated from $Fn1^{flox/+}$ or $Fn1^{flox/-}$ embryos at E14.5. $Fn1^{flox/-}$ MEFs were infected with adenoviruses encoding Cre recombinase, and sorted two days after infection, generating $Fn1^{\Delta/-}$ MEFs lacking Fn1. Deletion of Fn1 was confirmed using Western Blotting (data not shown). $3x10^4$ cells per well were plated in a 24-well plate on 1.2 mm glass coverslips without coating, and fixed with 4% PFA 72 hours later. Cells were stained with antibodies indicated to the left of the panels at 1:100 dilution. The same antibody solution was applied to $Fn1^{flox/+}$ and $Fn1^{\Delta/-}$ MEFs for each antibody. Primary antibodies were detected with anti-rabbit secondary antibodies conjugated with AlexaFluor-647 and imaged using identical settings. Signal intensity for stained $Fn1^{\Delta/-}$ cells was increased when making these panels to show background fluorescence. **B. 297.1 antibody reacts with bovine Fn1.** CM – complete medium as in Table M1. CCM – conditioned complete medium. CCM was prepared by incubating $2x10^5$ wild-type MEFs with 2 ml of CM for 48 hours in one well of a 6 well plate. Equal amount of medium was loaded in wells of Novex™ WedgeWell™ 4 to 12% Tris-Glycine protein gel. Arrow points at Fn1 band.